LES of Temporally Evolving Mixing Layers by an Eighth-Order Filter Scheme

A. Hadjadj*[,a], H.C. Yee[b], B. Sjögreen[c]

[a]*CORIA UMR 6614 & INSA de Rouen, 76800 St-Etienne du Rouvray, France*
[b]*NASA Ames Research Center, Moffett Field, CA, 94035, USA*
[c]*Lawrence Livermore National Laboratories, Livermore, CA, 94551, USA*

Abstract

An eighth-order filter method for a wide range of compressible flow speeds (H.C. Yee and B. Sjogreen, Proceedings of ICOSAHOM09, June 22-26, 2009, Trondheim, Norway) are employed for large eddy simulations (LES) of temporally evolving mixing layers (TML) for different convective Mach numbers (M_c) and Reynolds numbers. The high order filter method is designed for accurate and efficient simulations of shock-free compressible turbulence, turbulence with shocklets and turbulence with strong shocks with minimum tuning of scheme parameters. The value of M_c considered is for the TML range from the quasi-incompressible regime to the highly compressible supersonic regime. The three main characteristics of compressible TML (the self similarity property, compressibility effects and the presence of large-scale structure with shocklets for high M_c) are considered for the LES study. The LES results using the same scheme parameters for all studied cases agree well with experimental results of Barone et al. (2006), and published direct numerical simulations (DNS) work of Rogers & Moser (1994) and Pantano & Sarkar (2002).

Key words: DNS, LES, Homogeneous turbulence, Mixing layer, SWBLI

1. Motivation and Objective

For the last decade there has been an increase in the use of computational fluid dynamics (CFD) in engineering science, not only for fundamental understanding of complex compressible turbulent physics, but also for the development and design of industrial devices. Owing to the recent progress in petascale computing, in tandem with advances in algorithm development for accurate direct numerical simulations (DNS) and large eddy simulations (LES) of shock free compressible turbulence and turbulence with strong shocks, this type of DNS and LES computation has gradually been able to tackle more complex flows physics. Advances in flow visualization tools have paved the way to extracting valuable information from the computed results containing hundreds of terabytes of data. Examples include

*This work was performed while the first author was a visiting scholar at the Center for Turbulence Research, Stanford University.

flows through internal propulsive nozzles with shock-wave propagation or sound emission from supersonic jets, and mixing and shock/boundary layer interactions.

In compressible turbulent combustion/nonequilibrium flows, the constructions of numerical schemes for (a) stable and accurate simulation of turbulence with strong shocks, and (b) obtaining correct propagation speed of discontinuities for stiff reacting terms on "coarse grids" share one important ingredient - minimization of numerical dissipation while maintaining numerical stability. Here "coarse grids" means standard mesh density requirement for accurate simulation of typical non-reacting flows. This dual requirement to achieve both numerical stability and accuracy with zero or minimal use of numerical dissipation is most often conflicting for existing schemes that were designed for non-reacting flows. In addition to the minimization of numerical dissipation while maintaining numerical stability in compressible turbulence with strong shocks, Yee & Sjögreen, Yee and Yee & Sweby [65, 66, 62, 61, 68, 69] discussed a general framework for the design of such schemes. Yee & Sjögreen [70], Sjögreen & Yee [53] and Wei et al. [60] and references cited therein present their recent progress on the subject. In [73], a short overview of this recent progress is given. The discussion addresses three separate yet interwoven types of numerical challenges for high speed turbulent reacting flows containing discontinuities. This paper is confined to the study of turbulent mixing for non-reacting flows. The study for turbulent mixing for reacting flows is planned.

1.1. Recent Progress in Numerical Methods for Turbulence with Strong Shocks

The current trends in the containment of numerical dissipation in DNS and LES of turbulence with shocks are summarized in Yee & Sjögreen and Yee et al. [70, 69, 72]. See the cited references for details on these current trends. Before presenting the temporally evolving mixing layers (TML) studies, the key ingredients and the performance of the high order nonlinear filter schemes with pre-processing and post-processing steps in conjunction with the use of a high order non-dissipative spatial base scheme [70, 72] are briefly illustrated for two test cases.

1.1.1. High Order Nonlinear Filter Schemes [51, 68, 70, 72]

Before the application of a high order non-dissipative spatial base scheme, the preprocessing step to improve stability had split inviscid flux derivatives of the governing equation(s) in the following three ways, depending on the flow types and the desire for rigorous mathematical analysis or physical argument.

- Entropy splitting of Olsson & Oliger [38] and Yee et al. [64, 65]: The resulting form is non-conservative and the derivation is based on entropy norm stability with numerical boundary closure for the initial value boundary problem.

- The system form of the Ducros et al. splitting [12]: This is a conservative splitting and the derivation is based on physical arguments.

- Tadmor entropy conservation formulation for systems (Sjögreen & Yee [54]): The derivation is based on mathematical analysis. It is a generalization of Tadmor's entropy formulation to systems and has not been fully tested on complex flows.

After the application of a non-dissipative high order spatial base scheme on the split form of the governing equation(s), to further improve nonlinear stability from the non-dissipative spatial base scheme, the post-processing step of Yee & Sjögreen [68, 70], Sjögreen & Yee [51] nonlinearly filtered the solution by a dissipative portion of a high order shock-capturing scheme with a local flow sensor. These flow sensors provide locations and amounts of built-in shock-capturing dissipation that can be further reduced or eliminated. For all the computations shown, the Ducros et al. splitting is employed since a conservative splitting is more appropriate if one does not know if the subject flow is shock-free or turbulence with shocks. Some attributes of the high order filter approach are:

- Spatial Base Scheme: High order and conservative with high order freestream preservation metric evaluation for curvilinear grids. (no flux limiter or Riemann solver)
- Physical Viscosity: Automatically taken into consideration by the base scheme. The same order of central differencing for the viscous derivative as the convective flux derivatives are used.
- Efficiency: One Riemann solve per dimension per time step, independent of time discretizations (less CPU time and fewer grid points than their standard shock-capturing scheme counterparts)
- Accuracy: Containment of numerical dissipation via local wavelet flow sensor
- Well-balanced scheme: These nonlinear filter schemes are well-balanced schemes for certain chemical reacting flows and problem containing geometric source terms [59]
- Parallel Algorithm: Suitable for most current supercomputer architectures

1.2. Sample test Cases Illustrating the Efficiency and Accuracy of High Order Filter Schemes

These filter schemes are efficient, and the total computational cost for a given error tolerance is lower than for standard shock-capturing schemes of the same order. This is of importance, for example, in DNS and in flow control optimization to improve aerodynamic properties, where the flow simulation must be carried out many times during the optimization loop. The efficiency and accuracy of the schemes for a wide variety of flow problems can be found in aforementioned cited references. Here two test cases are illustrated.

2D Shock/Vorticity Interaction: Figure 1 shows a comparison of a second-order TVD, seventh-order WENO (WENO7), hybrid scheme (switch between eighth-order spatial central scheme and WENO7 using wavelet flow sensor as the switch indicator) and the filter

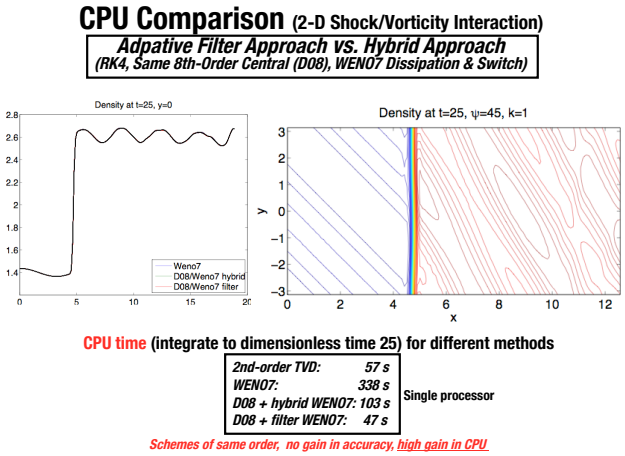

Figure 1: CPU comparison of four shock-capturing schemes.

scheme WENO7fi (an eighth-order spatial central base scheme and the dissipative portion of WENO7 and the same wavelet flow sensor to guide where the WENO7 dissipation should be applied at the post-possessing nonlinear filter step). A second-order Runge-Kutta method was used for the TVD scheme and the classical fourth-order Runge Kutta method was used for the rest of the spatial scheme. For this particular simple 2D shock-vorticity interaction test case with a simple weak planar shock without structure, WENO7, hybrid, and WENO7fi give the same accuracy. However, there is large gain in CPU time by the filter scheme for this turbulence-free test case. For turbulence with shocks, there is a more beneficial gain both in accuracy and CPU time of the filter schemes over the their standard WENO counterparts.

1D Shock/Turbulence Interaction Problem: This 1-D compressible inviscid ideal gas problem is one of the most computed test cases in the literature to assess the capability of a shock-capturing scheme in the presence of shock/turbulence interactions. The flow consists of a shock at Mach 3 propagating into a sinusoidal density field with initial data given by $(\rho_L,\ u_L,\ p_L) = (3.857143,\ 2.629369,\ 10.33333)$ to the left of a shock located at $x = -4$, and $(\rho_R,\ u_R,\ p_R) = (1+0.2\sin(5x),\ 0,\ 1)$ to the right of the shock, where ρ is the density, u is the velocity and p is the pressure. The computational domain is $[-5, 5]$ and the computation stops at time equal to 1.8. Figure 2 shows the comparison among WENO3, WENO5 and WENO7, and their corresponding filter schemes WENO3fi, WENO5fi and WENO7fi using a very coarse uniform grid of 200 points with the reference solution. The reference solution is obtained with WENO5 using 16000 grid points. WENO5fi required at the most 50% of the CPU time of WENO5 if third or fourth-order Runge-Kutta time discretization were used. In order for WENO5 to obtain a similar accuracy as WENO5fi, at least two times the number of grid points is needed. Moreover, the accuracy of WENO5fi is similar to WENO9 (computation not shown).

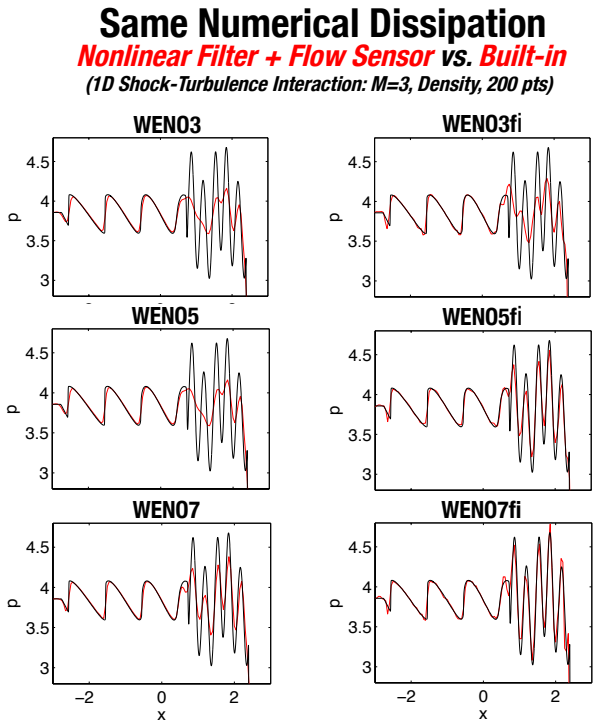

Figure 2:

1.3. Objective and Outline

In this paper we report recent studies of LES computations of compressible turbulent TML flows using numerical schemes developed by [51, 68, 70] in conjunction with the pre-processing step discussed previously. The current research is motivated by the overarching goal of developing numerical tools for reliable predictive capability of complex turbulent reacting flows, especially for problems including compressibility, heat transfer and real gas effects interacting with instabilities, shocks and turbulence. The comparative study among WENO7fi, WENO5 and WENO7 is reported in [71] with grid refinement studies was the first step in determining the suitable order of filter schemes to be used for the current physics based study. The LES filtering issue in the presence of shocks [47] is not addressed. The paper is organized as follows: Numerical methods are given in Section 2. The subgrid models for the compressible Navier-Stokes equations are given briefly in Section 3 and Appendix A. Results are then presented and discussed in Section 4.

2. Numerical Method

This section summarizes the numerical methods to be used for the turbulent TML study. The numerical methods solve the split form of the inviscid flux derivatives according to the pre-processing step. The discussion is broken up into two subsections.

2.1. Original High Order Filter Method

For turbulence with shocks, instead of solely relying on very high order high-resolution shock-capturing methods for accuracy, the filter schemes [63, 64, 51, 67, 68] take advantage of the effectiveness of the nonlinear dissipation contained in good shock-capturing schemes as stabilizing mechanisms at locations where needed. Such a filter method consists of two steps: a full time step using a spatially high-order non-dissipative base scheme, followed by a post-processing filter step. The post-processing filter step consists of the products of wavelet-based flow sensors and nonlinear numerical dissipations. The flow sensor is used in an adaptive procedure to analyze the computed flow data and indicate the location and type of built-in numerical dissipation that can be eliminated or further reduced. The nonlinear dissipative portion of a high-resolution shock-capturing scheme can be any TVD, MUSCL, ENO, or WENO scheme. By design, the flow sensors, spatial base schemes and nonlinear dissipation models are standalone modules. Therefore, a whole class of low dissipative high order schemes can be derived with ease. Unlike standard shock-capturing and/or hybrid shock-capturing methods, the nonlinear filter method requires one Riemann solve per dimension, independent of time discretizations. The nonlinear filter method is more efficient than its shock-capturing method counterparts employing the same order of the respective methods.

Recently, these filter schemes were proven to be well-balanced schemes [59] in the sense that these schemes preserve exactly certain steady state solutions of the chemical nonequilibrium governing equation. With this added property these filter schemes can better minimize spurious numerics in reacting flows containing mixed steady shocks and unsteady turbulence with shocklet components than standard non-well-balanced shock-capturing schemes. In addition, for some stiff reacting flow test cases, the high order filter scheme is able to obtain the correct propagation speed of discontinuities whereas the standard high order WENO scheme cannot [27, 74].

For simplicity of the presentation the discussion for the base scheme and post-processing step of the filter scheme is restricted to the inviscid part of the Navier-Stokes equations. For viscous gas dynamics the same order of spatial centered base scheme for the convection terms and the viscous terms are employed. For all of the LES computations the classical fourth-order Runge-Kutta time discretization is employed.

Consider the 3-D compressible Euler equations in Cartesian geometry,

$$U_t + \nabla \cdot \mathbf{F} = \mathbf{0};\; U = \begin{pmatrix} \rho \\ \mathbf{m} \\ e \end{pmatrix};\; \mathbf{F} = \begin{pmatrix} \rho\mathbf{u} \\ \rho\mathbf{u}\mathbf{u}^T + p \\ \mathbf{u}(e+p) \end{pmatrix}. \tag{1}$$

Here the velocity vector $\mathbf{u} = (u, v, w)^T$, the momentum vector $\mathbf{m} = (\rho u, \rho v, \rho w)$, ρ is the density, and e is the total energy.

In a Cartesian grid denote the grid indices for the three spatial directions as (j, k, l). The spatial base scheme to approximate the x inviscid flux derivatives $F(U)_x$ (with the grid

indices k and l for the y- and z-directions suppressed) is written as, e.g.,

$$\frac{\partial F}{\partial x} \approx D_{08} F_j, \tag{2}$$

where D_{08} is the standard eighth-order accurate centered difference operator. See [54] for the split form of 2.

After the completion of a full Runge-Kutta time step of the base scheme step, the second step is to adaptively apply a post-processing nonlinear filter. The nonlinear filter can be obtained e.g., in the x-direction by taking the full seventh-order WENO scheme (WENO7) [24] for the inviscid flux derivative in the x-direction and subtracting $D_{08}F_j$. The final update of the solution is (with the numerical fluxes in the y- and z-directions suppressed as well as their corresponding y- and z-directions indices on the x inviscid flux suppressed)

$$U^{n+1}_{j,k,l} = U^*_{j,k,l} - \frac{\Delta t}{\Delta x}[H^*_{j+1/2} - H^*_{j-1/2}]. \tag{3}$$

The nonlinear filter numerical fluxes usually involve the use of field-by-field approximate Riemann solvers. If the Roe type of approximate Riemann solver [43] is employed, for example, the x-filter numerical flux vector $H_{j+1/2}$ evaluated at the U^* solution from the base scheme step is

$$H_{j+1/2} = R_{j+1/2}\overline{H}_{j+1/2},$$

where $R_{j+1/2}$ is the matrix of right eigenvectors of the Jacobian of the inviscid flux vector in terms of the Roe's average states. Denote the elements of the vector $\overline{H}_{j+1/2}$ by $\overline{h}^l_{j+1/2}, l = 1, 2, ..., 5$. The nonlinear portion of the filter $\overline{h}^l_{j+1/2}$ has the form

$$\overline{h}^l_{j+1/2} = \frac{\kappa}{2}\omega^l_{j+1/2}\phi^l_{j+1/2}. \tag{4}$$

Here $\omega^l_{j+1/2}$ is the wavelet flow sensor to activate the nonlinear numerical dissipation $\frac{1}{2}\phi^l_{j+1/2}$ and the original formulation for κ is a positive parameter that is less than or equal to one. Some tuning of the parameter κ is needed for different flow types. A local κ to be discussed next, depending on the local Mach number for low speed flows and depending on local shock strength for high speed flows, would minimize the tuning of parameters. A local flow sensor was discussed by Lo et al. [32] by taking advantage of the Ducros et al. shock flow sensor [11] to obtain a local artificial compression method (ACM) sensor for the original Yee et al. filter scheme [63].

The dissipative portion of the nonlinear filter $\frac{1}{2}\phi^l_{j+1/2} = g^l_{j+1/2} - b^l_{j+1/2}$ is the dissipative portion of, e.g., WENO7 for the local lth-characteristic wave. Here $g^l_{j+1/2}$ and $b^l_{j+1/2}$ are numerical fluxes of WENO7 and the eighth-order central scheme for the lth characteristic, respectively. Hereafter, we denote this filter scheme as WENO7fi.

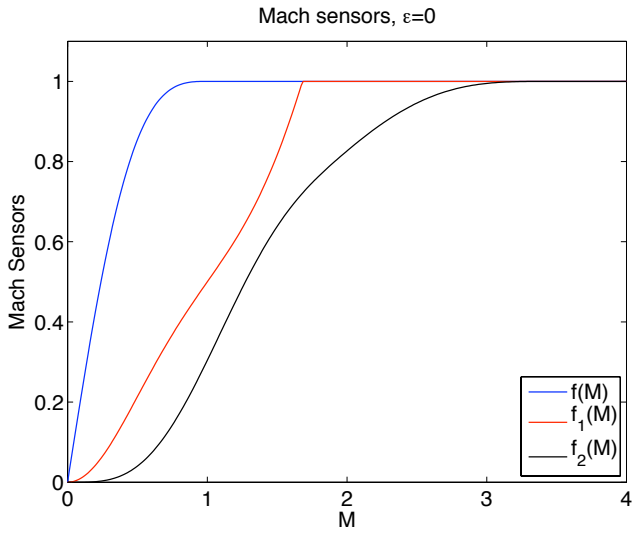

Figure 3: Mach number sensors. $f(M)$ (blue) function by Li and Gu, $f_1(M)$ (red) modified $f(M)$, and $f_2(M)$ (black) (includes low supersonic Mach numbers).

A summary of the three basic steps to obtain $\omega^l_{j+1/2}$ can be found in [51, 68]. For example, the flow sensor $\omega^l_{j+1/2}$ to activate the shock-capturing dissipation using the cut off procedure is a vector (if applied dimension-by-dimension) consisting of "**1's**" and "**0's**". For all of the computations, a three-level second-order Harten multiresolution wavelet decomposition of the computed density and pressure is used as the flow sensor [51].

2.2. Improved High Order Filter Method

Previous numerical experiments on a wide range of flow conditions [63, 64, 51, 67, 68] indicated that the original filter scheme improves the overall accuracy of the computation compared with standard shock-capturing schemes of the same order. Studies found that the improved accuracy is more pronounced if the parameter κ in (4) is tuned according to the flow type locally. For hypersonic flows with strong shocks, κ is set to 1. For high subsonic and supersonic flows with strong shocks, κ is in the range of $(0.3, 0.9)$. For low speed turbulent flows without shocks or long time integration of smooth flows, κ can be one to two orders of magnitude smaller than 1. In other words, κ should be flow location, shock strength and local flow type dependent. The improved κ proposed in [70] consists of a simple global κ for smooth flows and a local κ for problems with shocks and turbulence.

2.2.1. An efficient global κ for low Mach number and smooth flows:

The flow speed indicator formula of Li & Gu to overcome the shortcomings of "low speed Roe scheme" [30] was modified to obtain an improved global κ denoted by $\overline{\kappa}$ for (4) to minimize the tuning of the original κ for low Mach number flows. $\overline{\kappa}$ has the form:

$$\overline{\kappa} = f_1(M)\kappa, \tag{5}$$

with

$$f_1(M) = \min\left(\frac{M^2}{2}\frac{\sqrt{4+(1-M^2)^2}}{1+M^2}, 1\right). \tag{6}$$

Here M is the maximum Mach number of the entire computational domain at each stage of the time evolution. $f_1(M)$ has the same form as [30] except there is an extra factor "$\frac{M}{2}$" added to the first argument on the right-hand-side of the original form $f(M)$ in equation (18) of [30]. The added factor provides a similar value of the tuning κ observed from numerical experimentation reported in aforementioned cited references. With the flow speed indicator $f_1(M)$ in front of κ, the same κ used for the supersonic shock problem can be used without any tuning for the very low speed turbulent flow cases. Another minor modification of the above is,

$$\overline{f_1(M)} = \max\left(\min\left(\frac{M^2}{2}\frac{\sqrt{4+(1-M^2)^2}}{1+M^2}, 1\right), \epsilon\right),$$

where ϵ is a small threshold value to avoid completely switching off the dissipation. A function which retains the majority of $f_1(M)$ but includes larger Mach number for not very strong shocks is

$$f_2(M) = (Q(M,2) + Q(M,3.5))/2$$

or

$$\overline{f_2(M)} = \max((Q(M,2) + Q(M,3.5))/2, \epsilon),$$

where

$$Q(M,a) = \begin{cases} P(M/a) & M < a \\ 1 & \text{otherwise} \end{cases}.$$

The polynomial

$$P(x) = x^4(35 - 84x + 70x^2 - 20x^3)$$

is monotonically increasing from $P(0) = 0$ to $P(1) = 1$ and has the property that $P'(x)$ has three continuous derivatives at $x = 0$ and at $x = 1$.

Below supersonic speeds, a simple and efficient global $\overline{\kappa}$ can be obtained according to the maximum Mach number of the entire flow field and the value is determined by $f_1(M)$ or $f_2(M)$ for non-zero $\omega^l_{j+1/2}$. It is noted that if the original $f(M)$ were used instead of $f_1(M)$ or $f_2(M)$ in Eq.(5), the amount of nonlinear filter dissipation could be too large for very low speed turbulent flows (for the same fixed κ). See Fig. 3 for details.

2.2.2. Local flow sensor for a wide spectrum of flow speed and shock strength

At each time step and grid point, the aforementioned global $\overline{\kappa}$ is not sufficient to reduce the amount of numerical dissipation where needed for flows that contains a variety of flow features. A more appropriate approach is to obtain a"local κ" that is determined according to the above at each grid point. If known, a dominating shock jump variable should be used for shock detections. In other words, the filter numerical flux indicated in Eq.(4) is replaced by:

$$\overline{h}^l_{j+1/2} = \frac{1}{2}[\kappa^l_{j+1/2}\omega^l_{j+1/2}\phi^l_{j+1/2}]. \tag{7}$$

In the case of unknown physics and without experimental data or theory for comparison, $\kappa^l_{j+1/2}$ has to depend on the local Mach number in low speed or smooth flow regions, depend on local shock strength in shock regions and depend on turbulent fluctuations in vortical regions in order to minimize the tuning of parameters. According to the flow type locally, for each non-zero wavelet indicator $\omega^l_{j+1/2}$, $\kappa^l_{j+1/2}$ should provide the aforementioned amount (between $(0, 1)$) to be filtered by the shock-capturing dissipation $\phi^l_{j+1/2}$. For problems containing turbulence and strong shocks, the shock strength should come into play. One measure of the shock strength can be based on the numerical Schlieren formula [21] for the chosen variables that exhibit the strongest shock strength. In the vicinity of turbulent fluctuation locations, $\kappa^l_{j+1/2}$ will be kept to the same order as in the nearly incompressible case, except in the vicinity of high shear and shocklets.

Due to the fact that $\overline{\kappa}$ works well for local Mach number below 0.4, κ only needs to be modified in regions that are above 0.4. In other words, the final value of $\kappa^l_{j+1/2}$ is determined by the previous local $\overline{\kappa}$, if the local Mach number is below 0.4. If the local Mach number is above 0.4, at discontinuities detected by the non-zero wavelet indicator $\omega^l_{j+1/2}$, $\kappa^l_{j+1/2}$ is determined by the shock strength (normalized between $(0, 1)$) based on the Schlieren formula near discontinuities. Again, if known, dominating shock jump variables should be used for shock detections. At locations with turbulence, determined by the turbulent sensor (e.g., $\omega^l_{j+1/2}$ obtained from employing wavelets with higher order vanishing moments), $\kappa^l_{j+1/2}$ is kept to the same order as in the nearly incompressible case, except in the vicinity of high shear and shocklet locations, where a slightly larger $\kappa^l_{j+1/2}$ would be used. Methods in detecting turbulent flow can be (a) Wavelets with higher order vanishing moments, and (b) Wavelet based Coherent Vortex Extraction (CVE) of Farge et al. [15] (Split the flow into two parts: Active coherent vortices and incoherent background flow).

Results by the local $\kappa^l_{j+1/2}$ that take the local flow speed and shock strength into consideration will be reported in [72], an expanded version of [70]. Preliminary study with more complex shock turbulence problems and the applicability of even wider flow types indicates the necessity of the local $\kappa^l_{j+1/2}$.

3. LES implementation

In terms of turbulence modeling, there has been considerable progress in the development and usage of LES for the simulation of turbulent flows in the past few decades. This has been facilitated by the substantial increase in computing power. The triumphant journey of LES started with the pioneering work of Smagorinsky [55], Lilly [31], Deardoff [10], Germano [19] and others. Comprehensive accounts on LES are provided by Sagaut [46] and Pope [35, 42] and reviews at different stages of the development are provided by Rogallo and Moin [44], Galperin and Orszag [18], Lesieur and Metais [29], and Meneveau and Katz [34]. The LES model used for the current simulation is discussed here with subgrid model summaries in Appendix A.

In LES, the large-scale field can be obtained from the solution of the filtered Navier-Stokes equations, whereas scales smaller than the grid size are modeled. The filtering operation, which defines the large-scale variables (denoted by overbar), can be written as

$$\bar{\varphi}(\vec{x}) = \int_D G(\vec{x} - \vec{y}, \Delta)\, \varphi(\vec{y})\, d\vec{y},$$

where D is the flow domain, G is the filter function, and Δ is the filter-width associated with the wavelength of the smallest scale retained by the filtering operation.

For compressible flows, in order to avoid unclosed SGS terms in the continuity equation, a density-weighted Favre filter operator is introduced. This operator is defined as $\widetilde{\varphi} = \overline{\rho\varphi}/\bar{\rho}$.

Favre-filtered continuity, momentum and total energy equations in conservative form are respectively,

$$\frac{\partial \bar{\rho}}{\partial t} + \frac{\partial \bar{\rho}\, \widetilde{u}_i}{\partial x_i} = 0 \tag{8}$$

$$\frac{\partial \left(\bar{\rho}\, \widetilde{u}_i\right)}{\partial t} + \frac{\partial \left(\bar{\rho}\, \widetilde{u}_i \widetilde{u}_j\right)}{\partial x_j} + \frac{\partial \bar{p}}{\partial x_i} = \frac{\partial \breve{\sigma}_{ij}}{\partial x_j} - \frac{\partial \tau_{ij}}{\partial x_j} \tag{9}$$

$$\frac{\partial(\bar{\rho}\breve{E})}{\partial t} + \frac{\partial}{\partial x_j}\left[(\bar{\rho}\breve{E} + \bar{p})\widetilde{u}_j - \breve{\sigma}_{ij}\widetilde{u}_i + \breve{q}_j\right] = -\frac{\partial}{\partial x_j}\left(\mathcal{Q}_j - \mathcal{D}_j^v - \mathcal{J}_j + \frac{1}{2}\mathcal{E}_v\right) \tag{10}$$

Unlike the 'bar' and the 'tilde', the 'breve'-symbol does not denote a filter operation but indicates that the quantity is based on primitive filtered variables. Thus $\breve{E}$ refers to the resolved total energy, which is not equal to the filtered total energy. The resolved viscous stress tensor $\breve{\sigma}_{ij}$ and the heat flux are defined as

$$\breve{\sigma}_{ij} = 2\,\mu(\widetilde{T})\left(\widetilde{S}_{ij} - \frac{1}{3}\delta_{ij}\partial_k\widetilde{u}_k\right) \quad \text{with} \quad \widetilde{S}_{ij} = \left(\partial_j\widetilde{u}_i + \partial_i\widetilde{u}_j\right)/2$$

and

$$\breve{q}_j = -\lambda(\widetilde{T})\frac{\partial\widetilde{T}}{\partial x_j}$$

where $\mu(\widetilde{T})$ and $\lambda(\widetilde{T})$ are the viscosity and thermal conductivity corresponding to the filtered temperature $\widetilde{T}$. The constitutive equations are

$$\bar{\rho}\breve{E} = \frac{\bar{p}}{\gamma - 1} + \frac{1}{2}\bar{\rho}\widetilde{u_j}\widetilde{u_j} \quad \text{and} \quad \bar{p} = c_v(\gamma - 1)\bar{\rho}\widetilde{T}.$$

where heat capacity at constant volume, c_v, and the ratio of heat capacities, γ, are given constants. The subgrid scale stress is defined as

$$\tau_{ij} = \bar{\rho}(\widetilde{u_i u_j} - \widetilde{u}_i\widetilde{u}_j), \tag{11}$$

and the subgrid terms of the energy equation are

$$\mathcal{Q}_j = \quad \bar{\rho}\,\gamma\,c_v\left(\widetilde{u_j T} - \widetilde{u}_j\widetilde{T}\right) \tag{12}$$

$$\mathcal{J}_j = \quad \overline{q}_j - \breve{q}_j \tag{13}$$

$$\mathcal{D}_j^v = \quad \overline{\sigma_{jk}u_k} - \widetilde{\sigma_{jk}}\widetilde{u_k} \tag{14}$$

$$\mathcal{E}_j = \quad \overline{\rho}\left(\widetilde{u_j u_k u_k} - \widetilde{u}_j\widetilde{u_k u_k}\right). \tag{15}$$

We will model the subgrid terms in order to close the system. The model for the subgrid stress, τ_{ij}, employs the eddy viscosity hypothesis with an eddy viscosity, μ_t, with either a simple Smagorinsky model or a more advanced dynamic model. The details are given in Appendix A. In the energy equation, the subgrid terms $\mathcal{J}_j$, $\mathcal{D}_j^v$, and $\mathcal{E}_j$ are set equal to zero, and the subgrid scale heat flux is modeled using the eddy diffusivity hypothesis,

$$\mathcal{Q}_j = -\frac{\mu_t\gamma c_v}{Pr_t}\frac{\partial\widetilde{T}}{\partial x_j},$$

where the turbulent Prandtl number, Pr_t, is a given constant.

4. LES of Temporally Evolving Compressible Mixing Layers (TML)

In this section, employing WENO7fi, LES of temporally evolving mixing layers between two streams moving with opposite velocities is considered, with $U_1 = -U_2 = \Delta U/2$. From here on, WENO7fi refers to the pre-processing step (Ducros et al. splitting of the inviscid flux derivative) in conjunction with the eighth-order central spatial base scheme with the dissipative portion of WENO7 and the global flow sensor discussed in Section 2 with $\kappa = 0.7$. The three main characteristics of compressible mixing layers are: 1) the self similarity property, which is characterized by linear growth of the layer width as well as the mean velocities and turbulent statistics being independent of the downstream distance when normalized by appropriate length and velocity scales, 2) the compressibility effects through the turbulence damping and the decrease of the mixing-layer growth rate for high convective Mach numbers, and 3) the presence of large-scale structure with shocklets. These organized structures play an important role in the dynamics of the mixing layer, its spreading and energy transport. The objective of the current investigation is to verify that WENO7fi used in this study is capable of capturing the three-key points cited above.

4.1. Problem Setup

The configuration of the TML is shown in Fig. 4. Five test cases (denoted LES-C$_i$, $i = 1, .., 5$) are carried out with different convective Mach numbers (M_c) ranging from the incompressible case $M_c = 0.1$ up to the supersonic one $M_c = 1.5$. The latter corresponds to a highly compressible mixing layers, whereas the first two cases $M_c = 0.1$ and $M_c = 0.3$ can be considered as quasi-incompressible and are used to compare with the experimental results of an incompressible shear layer. All of the simulations described below are performed at an initial Reynolds number, Re_{ω_0}, based on the mean velocity difference ΔU, the average viscosity of the free streams and the vorticity thickness δ_{ω_0} of 800 with $\delta_{w_0} = 4\,\delta_{\theta_0}$, where $\delta_\omega = \Delta U / \langle \partial u / \partial y \rangle_{max}$ is the vorticity thickness of the shear layer, and δ_θ is the momentum thickness given by Eq. 17 (see later section). It is worth noticing that Re_ω reaches values as large as 3×10^5 at the end of the simulation, which is one order of magnitude higher than similar DNS and LES computations reported in the literature [39, 33, 16]. Table 1 summarizes the detail of flow parameters for both LES and previous DNS data of the literature. The mean flow is initialized with a tangent hyperbolic profile for the streamwise velocity, $u(y) = \frac{1}{2}\Delta U \tanh\left[y/(2\,\delta_{\theta_0})\right]$, while the two other velocity components are set to zero. In addition to these mean values, three-dimensional turbulent fluctuations (u', v', w') are imposed, while initial pressure and density are set constant. Since the simulation is temporal, the initial velocity perturbations are computed using a digital filter technique [26]. This procedure utilizes the prescribed Reynolds stress tensor and length scales of the problem concerned to generate the corresponding fluctuating velocity field, taking into account the nature of the autocorrelation function for the prevailing turbulence. The digital filter algorithm is given in Appendix B. The length scales are chosen as δ_{w_0} in each direction. The Reynolds stresses have a Gaussian shape in y with amplitudes chosen to be similar to the experimental peak intensities observed in incompressible mixing layer [5].

Periodic boundary conditions are enforced in the streamwise (x) and spanwise (z) directions, while non-reflecting conditions are applied at both top and bottom boundaries (y direction). The use of a periodic boundary condition in the x direction corresponds to the temporal formulation of mixing layer evolution, which evolves only in time as it spreads in y.

4.2. Mesh Requirements

Similar to [16], a computational domain of lengths $L_x \times L_y \times L_z = 1200\,\delta_{\theta_0} \times 370\,\delta_{\theta_0} \times 270\,\delta_{\theta_0}$ is used with the corresponding mesh points $N_x \times N_y \times N_z = 512 \times 211 \times 131$. The same grid system uniformly spaced in the x and z directions and stretched in the y direction is employed for all considered cases. The stretching function for the y-direction is based on $\frac{L_y}{2}\frac{\sinh(b_y\eta)}{\sinh b_y}$, where L_y is the box size in the y-direction and the stretching factor $b_y = 3.4$. The mapped coordinate η is equally spaced and runs from -1 to 1. The high resolution (HR) grid used in this study contains an order of magnitude fewer cells than that of the DNS of Pantano and Sarkar [39] compared to the domain length. The emphasis of the HR simulation is to produce an LES solution that predicts the trends of the DNS as well as experimental data for both quasi-incompressible and highly compressible mixing layers.

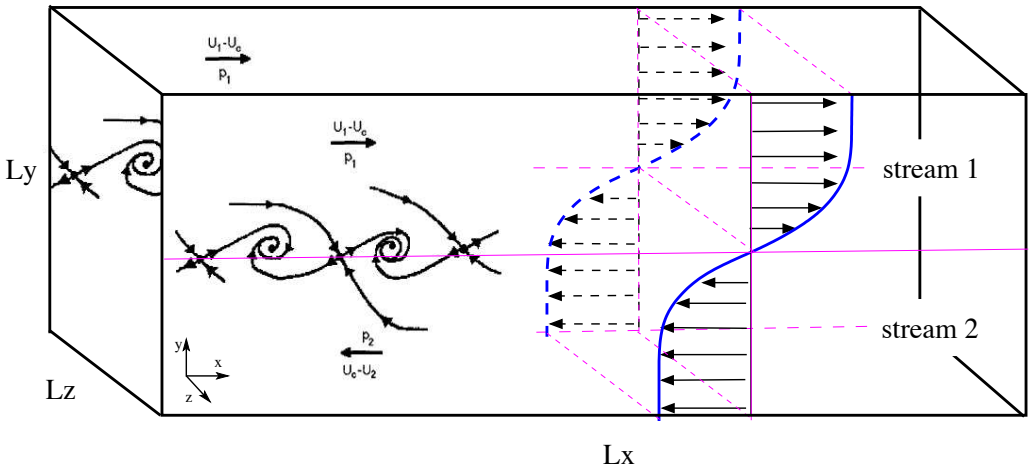

Figure 4: Schematic configuration of temporal mixing layer

To ensure that the computational domain in the x- and z-directions is sufficiently wide, the two-point correlation functions are analyzed

$$R_{\varphi\varphi}(r) = \sum_{k=1}^{N-k_r} \overline{\varphi'_k \, \varphi'_{k+k_r}}, \qquad k_r = 0, 1, ..., N-1, \tag{16}$$

where $r = k_r \Delta$, N is half of the number of grid points in the homogeneous directions with grid size Δ and φ' represents the fluctuations of flow variables.

The computed two-point autocorrelation coefficients $R_{\varphi\varphi}(r)/R_{\varphi\varphi}(0)$ (pressure as well as velocity components) in the homogeneous directions (x and z) are reported in Fig. 5 as a function of the distance in the stream- and spanwise coordinates at the middle of the mixing layer ($L_y/2$). This figure shows that the flow variables are sufficiently decorrelated over distances $L_x/2$ and $L_z/2$, thus ensuring that the streamwise as well as the spanwise extents of the computational domain are sufficient to not inhibit turbulence dynamics. Also, the length in the y direction is selected to be large enough for the flow to achieve a fully developed state before the effects of the upper and lower boundaries are felt. In terms of turbulent length scales, the Kolmogorov length scale η and an average (isotropic) Taylor micro-scale λ are defined as $\eta = (\nu^3/\varepsilon)^{1/4}$ and $\lambda = \sqrt{15\,\nu\,k/\varepsilon}$, where $k = \frac{1}{2}(\overline{u'^2} + \overline{v'^2} + \overline{w'^2})$ is the turbulent kinetic energy. The computed integral length scales (Λ_x, Λ_z) and the Kolmogorov scale are also given in Table 1 for further comparison. In our case the integral scales are given by

$$\Lambda_x = \int_0^{L_x/2} \frac{\langle u_i(x_i,t)\, u_i(x_i+p,t)\rangle}{\langle u_i^2\rangle} dp, \qquad \Lambda_z = \int_0^{L_z/2} \frac{\langle u_i(x_i,t)\, u_i(x_i+p,t)\rangle}{\langle u_i^2\rangle} dp,$$

where p is the distance between two points in the flow. The integral length scale is important in characterizing the structure of turbulence. It is a measure of the longest correlation

Table 1: Flow parameters and turbulent length scales during the quasi-self-similar stage.

Case	M_c	Re_{ω_0}	L_x/Λ_x	L_z/Λ_z	$\Delta y_{min}/\lambda$	$\Delta y_{min}/\eta$
DNS [45]	0	800	–	–		
DNS [39]	0.3	640	20.4	15.3	> 1	≈ 1
LES-C1	0.1	800	30.2	15.1	0.64	49.3
LES-C2	0.3	800	30.2	15.1	0.65	49.5
LES-C3	0.8	800	12.1	11.0	0.74	50.1
LES-C4	1.0	800	12.0	11.4	0.67	53.7
LES-C5	1.5	800	12.0	10.2	0.82	55.2

distance between the flow velocity (or vorticity, etc) at two points in the flow field. Recent work concludes that a reasonable lower limit on the domain must be at least six times larger than the integral length [37]. This recommendation is consistent with the data shown in Table 1, where the spatial domain is between ten and thirty times larger than the integral length. Also, it is evident from Table 1 that the integral lengths are sufficiently small compared to the computational domain and the grid resolution is adequate to resolve the large scales of turbulence.

Owing to the high computational cost of the simulations, the numerical code is fully parallelized running on up to 600 processors. In total, the present simulation required 2000 CPU hours each on modern SGI IC, Pleiades and Columbia supercomputers at NASA Ames Research Center.

4.3. Mean Flow and Turbulent Statistics

LES computations are carried out up to dimensionless time $\tau = t\Delta U/\delta_{\theta_0} \simeq 3000$ for the higher convective Mach number cases and $\tau \simeq 1200$ for the quasi-incompressible cases. In order to compare the LES results with experimental data, the time averaged flow quantities $\langle\overline{\varphi}\rangle$ and $\langle\widetilde{\varphi}\rangle$ are extracted from the flow field during the self-similar time period ($600 < \tau < 1000$ for LES-C1 and LES-C2 and $2000 < \tau < 2800$ for LES-C3, LES-C4 and LES-C5). Note that throughout this paper only resolved quantities are considered; subgrid-scale contributions are not added onto e.g. the turbulent stresses. To validate the low-Mach-number LES case, previous DNS studies of the incompressible shear layer, including Rogers and Moser [45], Pantano and Sarkar [39], as well as experimental studies by Bell and Mehta [5] and Spencer and Jones [56], are used. Further experimental results on the compressible shear layer (Papamoschou and Roshko [40], Elliot and Samimy [13], Barre et al. [4], Chambres et al. [8]) and DNS results obtained by Pantano and Sarkar [39] are used to compare with the high-Mach-number simulations.

As recommended by Rogers and Moser [45], the momentum thickness δ_θ is used for self-similar scaling rather than the vorticity thickness δ_ω, because it is less sensitive to statistical noise as it is an integral quantity evolving smoothly in time, while δ_ω is obtained

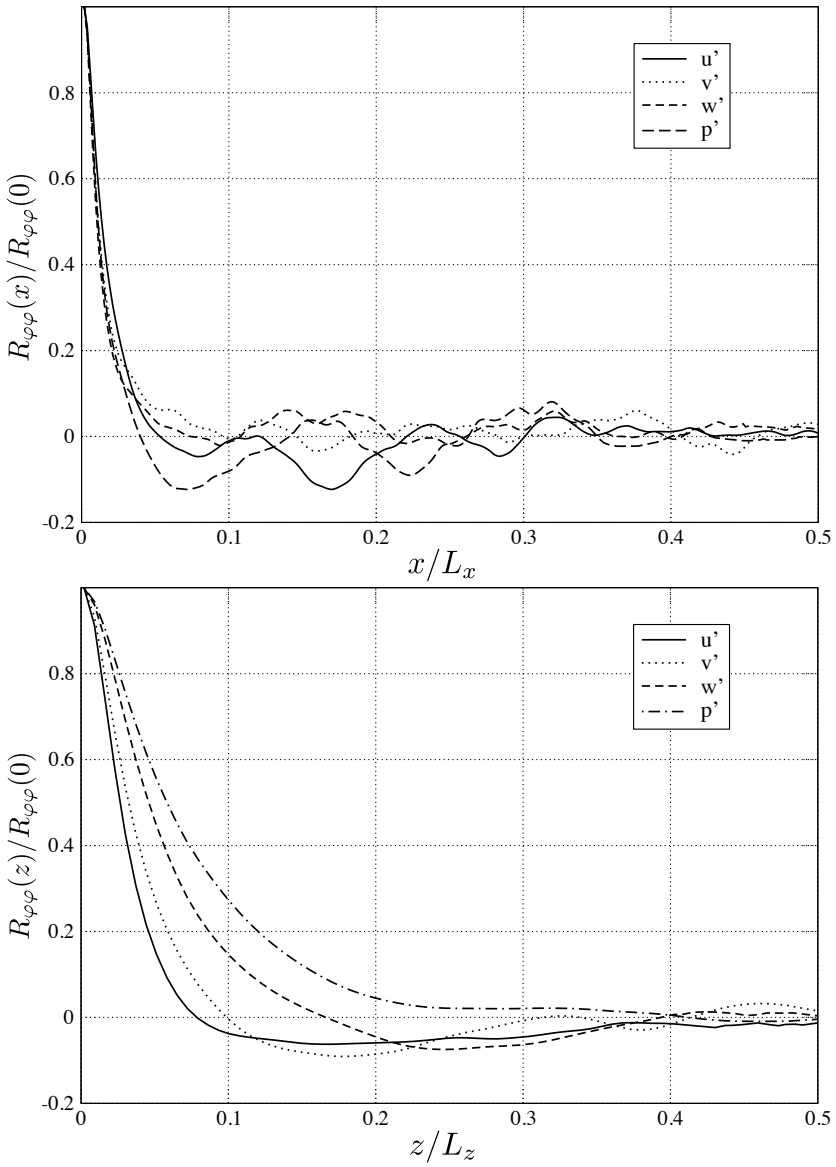

Figure 5: Streamwise and spanwise autocorrelation functions for LES-C5.

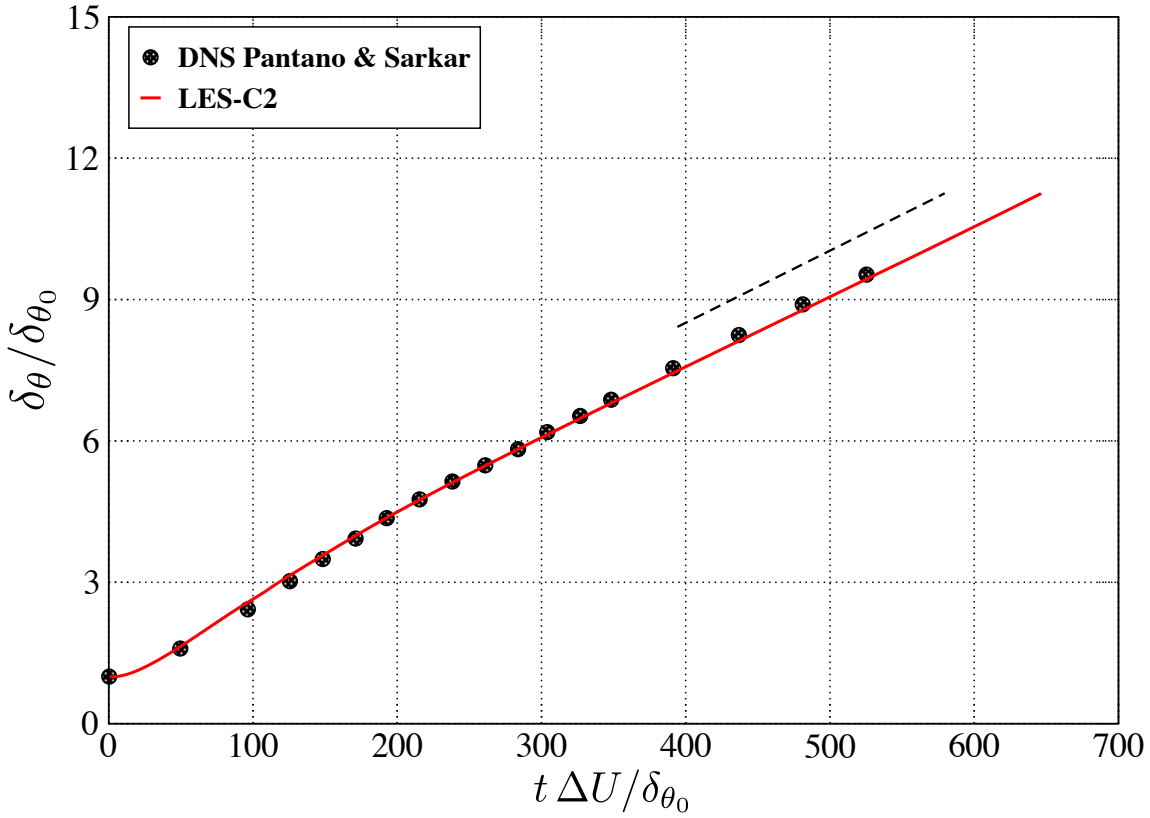

Figure 6: Time evolution of normalized momentum thickness for LES-C2 compared to the DNS of Pantano & Sarkar [39] for $M_c = 0.3$.

from the derivative of the mean velocity and may exhibit oscillations during the flow evolution. Therefore, the time evolution of the momentum thickness of the flow calculated using the definition

$$\delta_\theta = \int_{-\infty}^{+\infty} \frac{\overline{\rho}}{\rho_{ref}} \left(\frac{1}{4} - \frac{\widetilde{u}^2}{\Delta U^2} \right) dy \tag{17}$$

is shown in Fig. 6. Excellent agreement with the DNS simulation is obtained and the linear slope is recovered after a short transient, showing the self-similar state of the mixing layer. The growth rate $d(\delta_\theta/\delta_{\theta_0})/d\tau = 0.016$ (slope of the linear curve fit). The ratio of vorticity thickness to momentum thickness is $D_\omega = \delta_\omega/\delta_\theta \simeq 4.5$ with $Re_\omega = 603391$ at $\tau_{max} \simeq 1200$. This is in excellent agreement with the DNS growth rate of quasi-incompressible case with $M_c = 0.3$ of Pantano & Sarkar [39]. Note that in Eq. 17, $(\,)_{ref}$ represents the reference state which is the arithmetic mean of the free stream 1 and 2.

The normalized mean streamwise velocity for LES-C1 and LES-C2 are presented in Fig. 7. It can be seen that the two LES profiles collapse together and are in excellent agreement with both DNS [39] and experimental results [5, 56].

Further validation of the present LES is achieved through the comparison of turbulent intensities in the self-similar region (calculated by averaging over profiles plotted in similarity coordinates) seen in Fig. 8, where different components of the normalized Reynolds stress tensor, $\sqrt{R_{ij}}/\Delta U$ ($R_{ij} = \overline{\rho u_i'' u_i''}/\overline{\rho}$), are compared to DNS and experimental data. Interestingly, at $Mc = 0.1$ the LES agrees better with experimental [5, 56] and DNS [45] data in the incompressible shear layer than the DNS results of Pantano & Sarkar [39]. Table 2 summarizes the comparison of peak turbulent intensities, as well as the anisotropic deviation on the centerline of the layer. It is evident that very good agreement between the present LES and previous results is obtained for this measure of anisotropy. It is important to notice that both LES-C1 and LES-C2 give almost the same results, probably because both are in the incompressible (or weakly-compressible) regime.

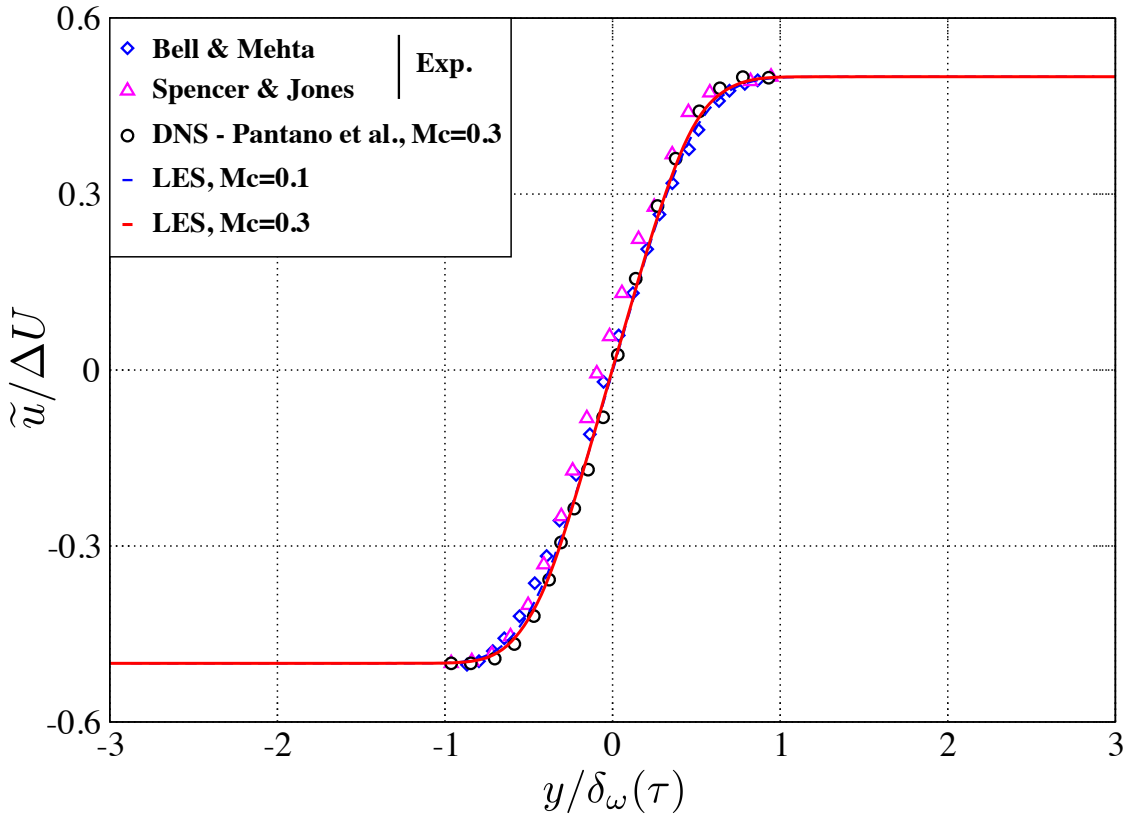

Figure 7: Comparison of normalized mean streamwise velocity for LES-C1 and LES-C2.

4.4. Compressibility Effects

Apart from studying the self-similarity property in the mixing layer, effects of convective Mach number are also investigated using LES. Fig.9 shows the time evolution of momentum thickness for various convective Mach numbers. It can be seen that after a relatively long time ($\tau > 2000$ compared to the incompressible one), corresponding to the initial transient, the mixing layer grows quasi-linearly with spread rates of

Table 2: Comparison of peak turbulent intensities of incompressible mixing layer

	Bell et al.	Pantano et al.	LES-C1 / LES-C2
M_c	0	0.3	0.1 / 0.3
$\sqrt{\langle R_{11}\rangle}/\Delta U$	0.18	0.155	0.17
$\sqrt{\langle R_{22}\rangle}/\Delta U$	0.14	0.134	0.134
$\sqrt{\langle R_{33}\rangle}/\Delta U$	0.146	0.143	0.143
$\sqrt{\langle R_{12}\rangle}/\Delta U$	0.10	0.103	0.106
$\sqrt{\langle R_{22}\rangle/\langle R_{11}\rangle}$	0.777	0.788	0.788
$\sqrt{\langle R_{12}\rangle/\langle R_{11}\rangle}$	0.555	0.606	0.623

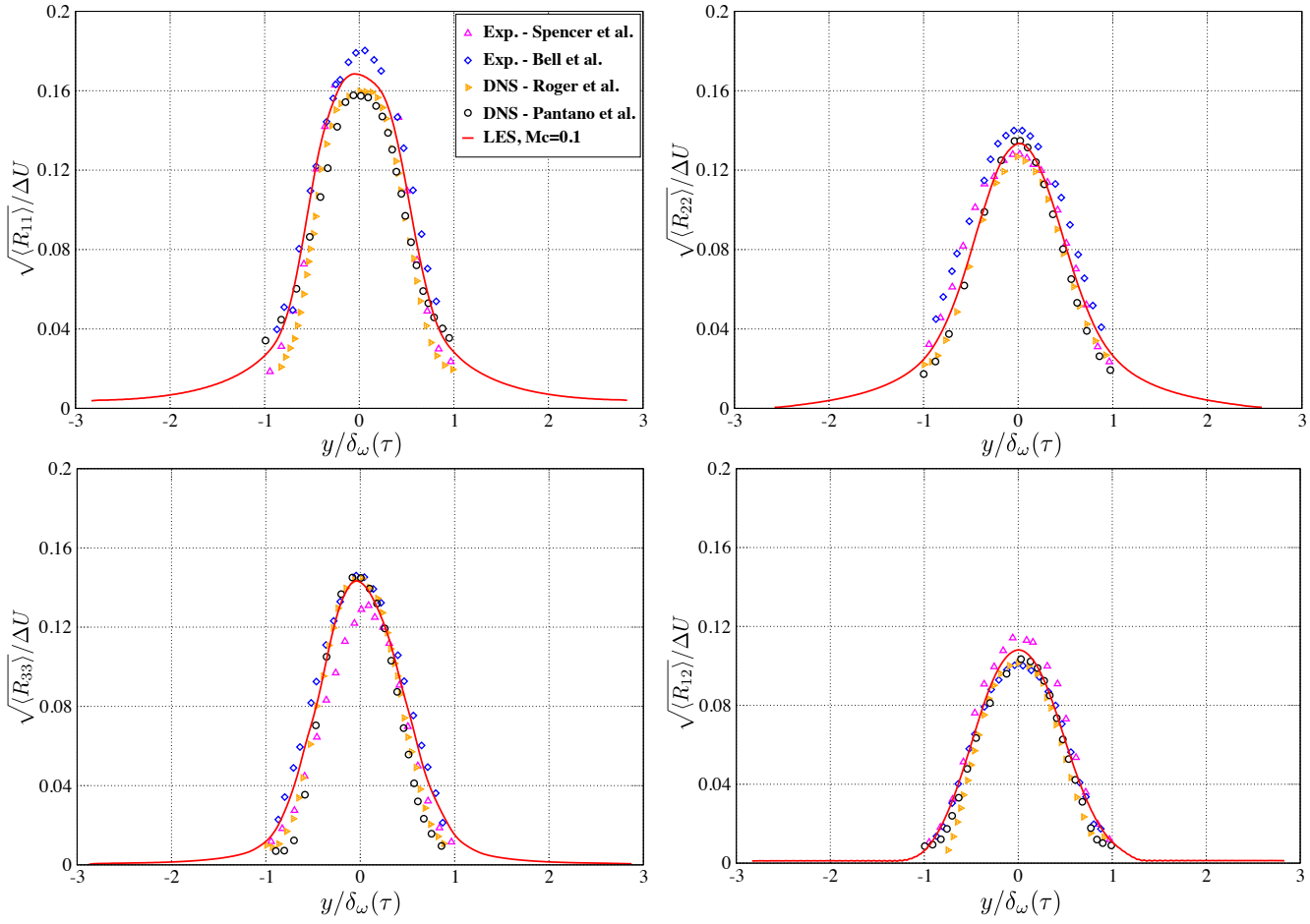

Figure 8: Comparison of the normalized Reynolds stress tensor, $R_{ij} = \langle \rho u_i' u_j' \rangle / \langle \rho \rangle$.

$d(\delta_\theta/\delta_{\theta_0})/d\tau = 0.0165\,, 0.0101\,, 0.0084$ and 0.0075 for cases LES-C2, LES-C3, LES-C4 and LES-C5, respectively.

In compressible mixing layers, all of the assessments of compressibility effects can be related to the convective Mach number, M_c, through the compressibility factor, $\Phi = (d\delta/d\tau)_c/(d\delta/d\tau)_i$, which is the ratio of the compressible growth rate to the incompressible growth rate at the same velocity and temperature ratios. The calculated compressibility factor is significantly less than one (the incompressible counterpart), the ratio of the two being less than 0.43 for $M_c > 1$. This is consistent with previous findings on the effects of compressibility on mixing-layer growth rate such as the nonlinear regression fit of Barone [3, 28] plotted in Fig. 10. This plot shows the ratio of compressible mixing-layer growth to incompressible mixing-layer growth rate as a function of M_c, and data from different experiments and previous DNS have been included for comparison. The three higher compressibility cases have growth rates that agree well with previously published data. As already pointed out by Papamoschou [41], the growth-rate reduction starts at subsonic values of M_c and is evidently completed before M_c becomes supersonic (Fig. 10). This implies that compressibility takes effect before any shock or expansion waves appear in the flow, in the convective frame of reference.

It is worth noticing that the data in this figure exhibit significant scattering that is partly attributable to the different experimental conditions. As pointed out by Barone et al. [3], one can mention that future investigations should be conducted at higher convective Mach numbers to better determine the asymptotic value of Φ.

Also, the dependence of the turbulent kinetic energy of the shear layer on M_c is shown in Fig. 11. The simulations show that the turbulence intensity decreases with increasing convective Mach number. The decreased level of energy is responsible for the reduction of the mixing thickness growth rate as already pointed out by Samimy [49], Vreman et al. [58] and many other LES and DNS studies [39, 16, 50].

4.5. Flow Structures and Shocklets

The invariant of velocity gradient tensor $\mathbf{Q}$ and the corresponding normalized form $\mathbf{\Lambda}$ are defined by

$$\mathbf{Q} = \frac{1}{2}\left[\Omega_{ij}\Omega_{ij} - S_{ij}S_{ij}\right], \quad \mathbf{\Lambda} = \frac{\left[\Omega_{ij}\Omega_{ij} - S_{ij}S_{ij}\right]}{\left[\Omega_{ij}\Omega_{ij} + S_{ij}S_{ij}\right]}, \tag{18}$$

where $S_{ij} = \left(u_{i,j} + u_{j,i}\right)/2, \quad \Omega_{ij} = \left(u_{i,j} - u_{j,i}\right)/2.$

The iso-surfaces of $\mathbf{Q}$ and $\mathbf{\Lambda}$ are plotted for flow visualization of mixing layers. It is evident that the positive values of $\mathbf{Q}$ and $\mathbf{\Lambda}$ represent the vortex dominated portion of the flow. Three-dimensional perspective views of iso-surfaces of $\mathbf{Q}$ are presented in Fig.12 for LES-C2 in a self-similar state. The 3D complex vortex tube structures are clearly evident from these figures.

With regard to the highly compressible case $M_c = 1.5$, the complexity of three-dimensional flow structure leads to difficulties in the identification of shocklets. One good

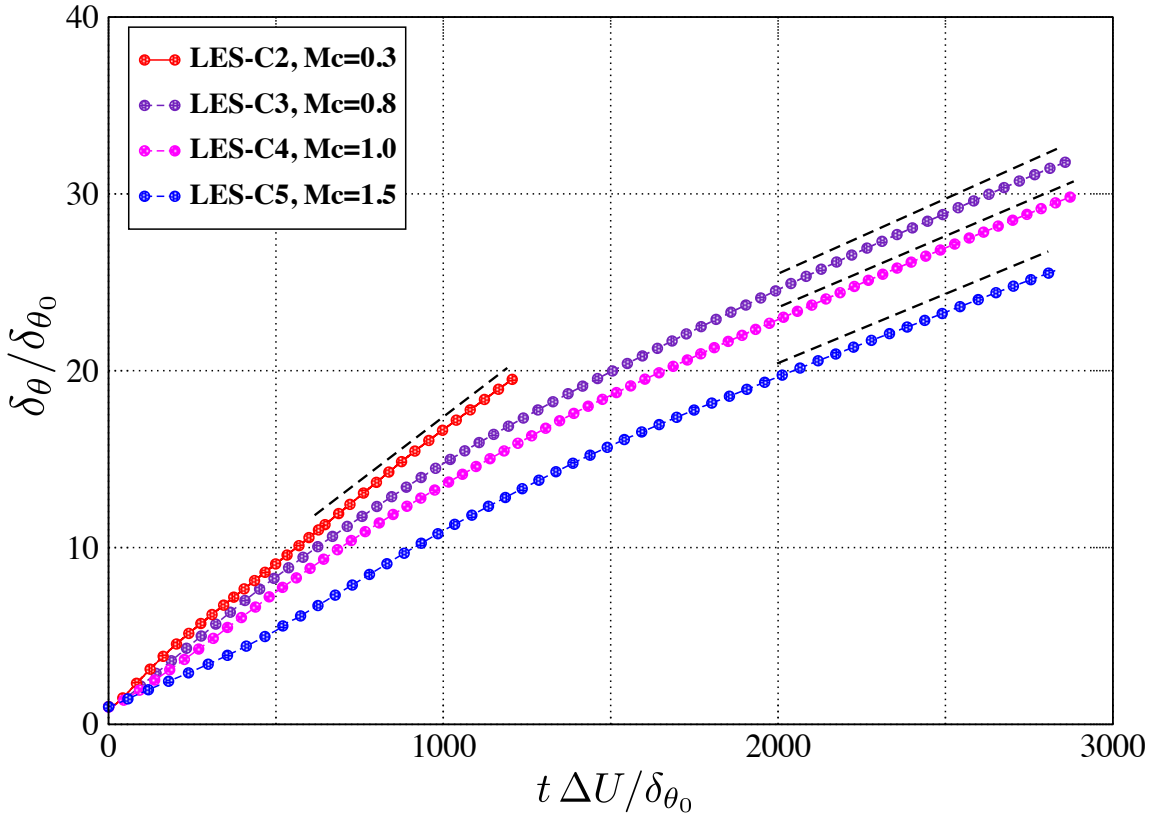

Figure 9: Time evolution of normalized momentum thickness for LES at different convective numbers.

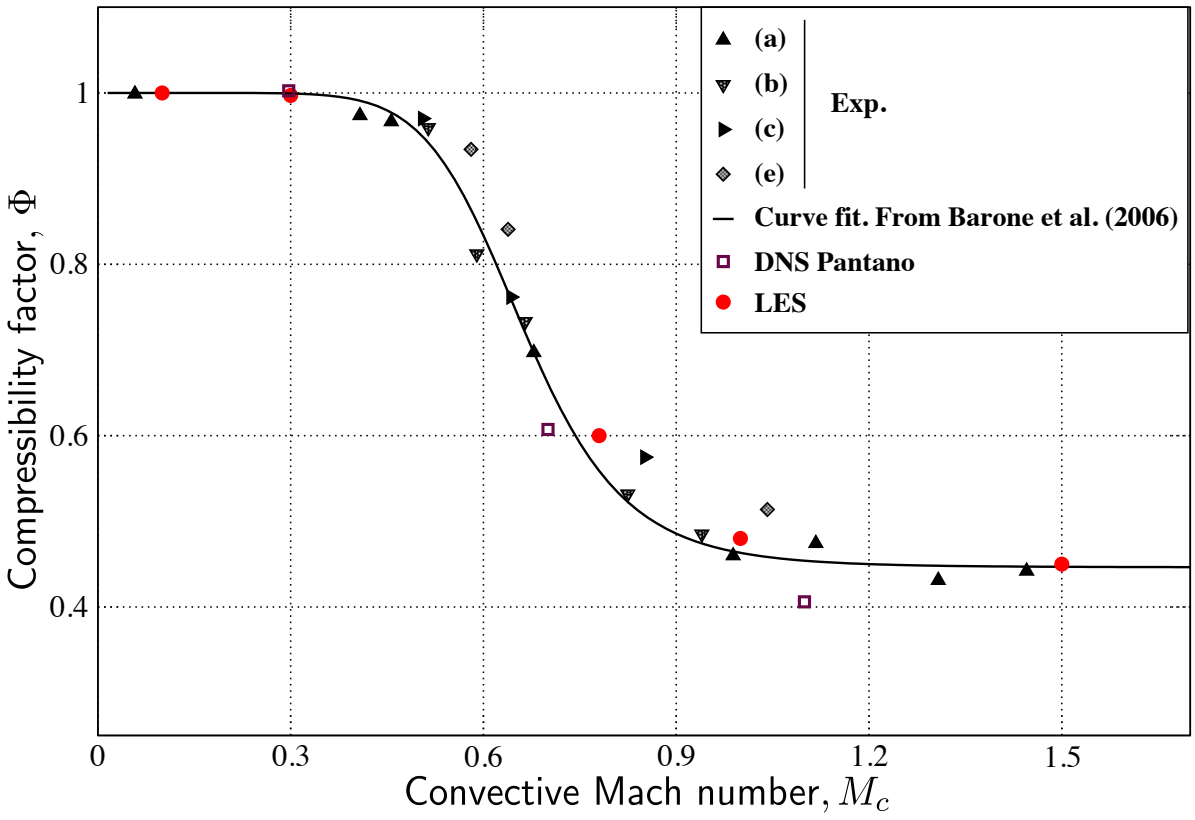

Figure 10: Temporal mixing: Compressibility factor as function of the convective Mach number from different experimental mixing-layer studies selected by Barone et al. [3]: (a) Bogdanoff [7]; Papamoschou and Roshko [40]; (b) Chinzei at al. [9]; (c) Samimy and Elliott [48, 49]; — nonlinear regression curve from [3] with $\Phi(M_c) = 1 - a_1\,[1 - 1/(1 + a_2 M_c^{a_3})]$, $a_1 = 0.5537$, $a_2 = 31.79$, $a_3 = 8.426$. (d) Gruber et al. [20]. LES computations by WENO7fi (red solid circles) for $M_c = 0.1, 0.3, 0.8, 1.0, 1.5$.

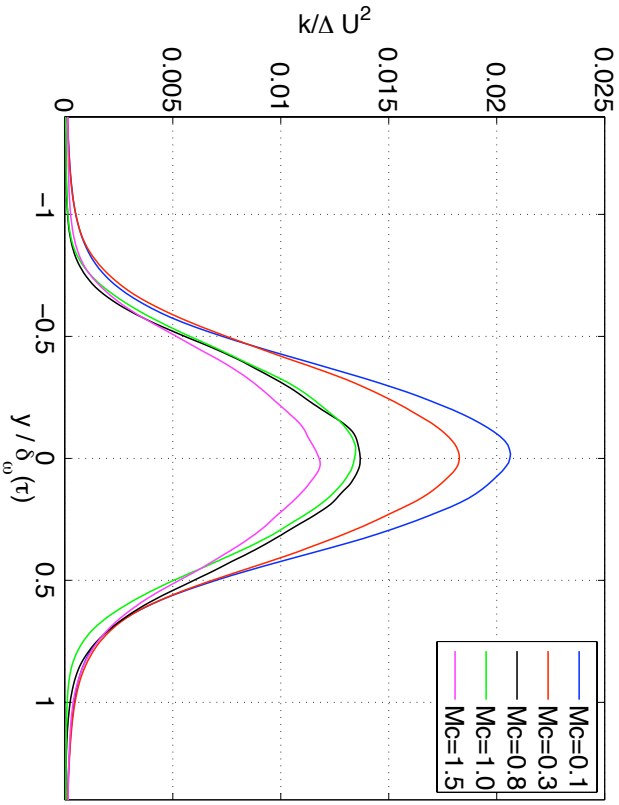

Figure 11: Normalized turbulent kinetic energy at different convective Mach numbers.

method to identify the location of a shock is to use a Schlieren based technique to portray shocks and even more weak discontinuities in the fluid (see ref. [21] for more details about flow visualization). Since, in our case, the initial density is uniform, we used Schlieren based on the dilatation of the velocity field $\nabla \mathbf{u}$ to highlight the eddy shocklets (see Fig. 14). Note that shocklets start to appear at Mach number less than unity, i.e. in the lower part of the transonic regime. As expected, for higher Mach numbers the shocklets become stronger and are preferentially organized in oblique waves (see Fig. 14), corresponding to stationary inviscid shocks at a dominant propagation directions, θ, and a nominal Mach number, $M_n = \Delta U/(2c)$, where c is the speed of sound in the unperturbed region. Avital et al. [1, 2] provide a correlation to find the propagation angle corresponding to the most perturbed waves. It is given by $M_c \cos\theta = 0.6$. Therefore for $M_c = 1.5 \rightarrow \theta_{th} = 66^\circ$. In our case, a visual measurement of the oblique wave angle gives an approximate value of $\theta_{sim} \simeq 65^\circ$, which is very close to the predicted value.

From the present computation it can be seen that oblique structures start to occur at convective Mach numbers less than unity. These structures are related to compression waves emanating from the shear layer and also the existence of other perturbing pressure disturbances and lead to enhanced mixing through the creation of streamwise vortices.

5. Concluding Remarks

This paper illustrates some recent progress in computations of compressible turbulence using a high-order spatial scheme on a LES model for temporally evolving turbulent mixing layers. Results obtained including flow visualization, streamwise velocities, fluctuating velocities and Reynolds stresses agree well with experimental results. The current LES agree with the previous DNS of the mixing layer by Vreman et al. [58] and Freund et al. [17] that show decreased turbulence production with increasing M_c.

The present study serves as a validation and performance of the improved filter schemes of [70] on a representative complex compressible turbulent flow consisting of a wide range of flow speeds. All the computations use the Ducros et al. splitting of the inviscid flux derivatives and WENO7fi with $\overline{\kappa}$ and $\kappa = 0.7$ described in Section 2.2.1. In all M_c cases, no tuning of WENO7fi scheme parameters were needed. LES comparison among WENO7fi, WENO5 and WENO7 for the TML is reported in [71]. Studies indicated that WENO7fi compared well with experimental data and published DNS work. For all the considered M_c cases, solutions by WENO5 and WENO7 compared poorly with experimental data and DNS computations. The comparative study among WENO7fi, WENO5 and WENO7 is reported in [71] was the first step in determining the suitable order of filter schemes to be used for the current physics based study.

The same high order filter scheme is being used for the simulation of two much higher M_c cases of $M_c = 2, 3$. The computational box size, especially in the y-direction has to be doubled or more. A finer grid is also needed in order to obtain an accurate and stable solution. These computations are many times more CPU-intensive than the lower M_c cases. Results will be reported in a forthcoming paper.

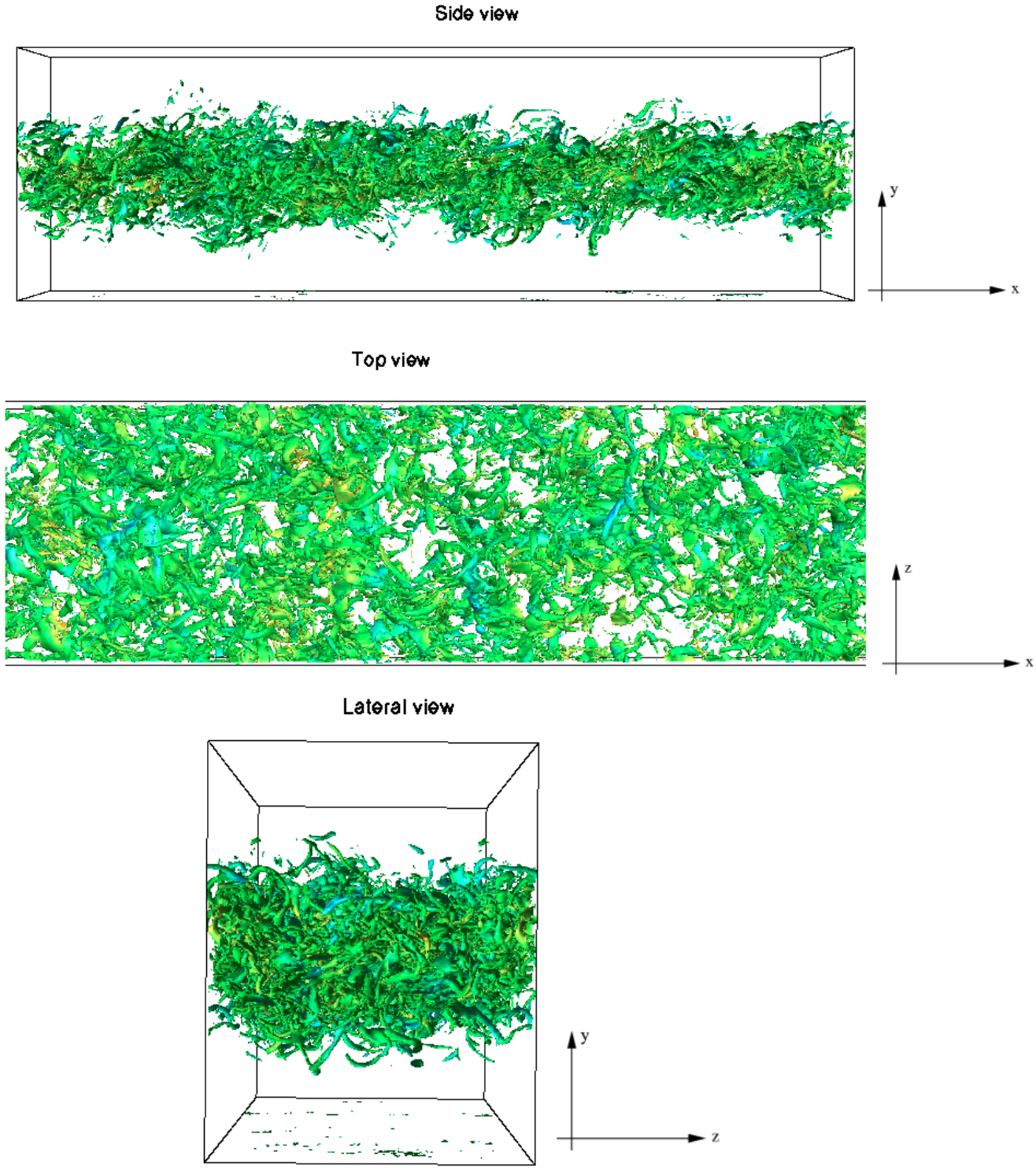

Figure 12: Iso-surfaces of $\mathbf{Q} = 0.01, \mathbf{Q}_{max}$ at $\tau = 1000$, LES-C2.

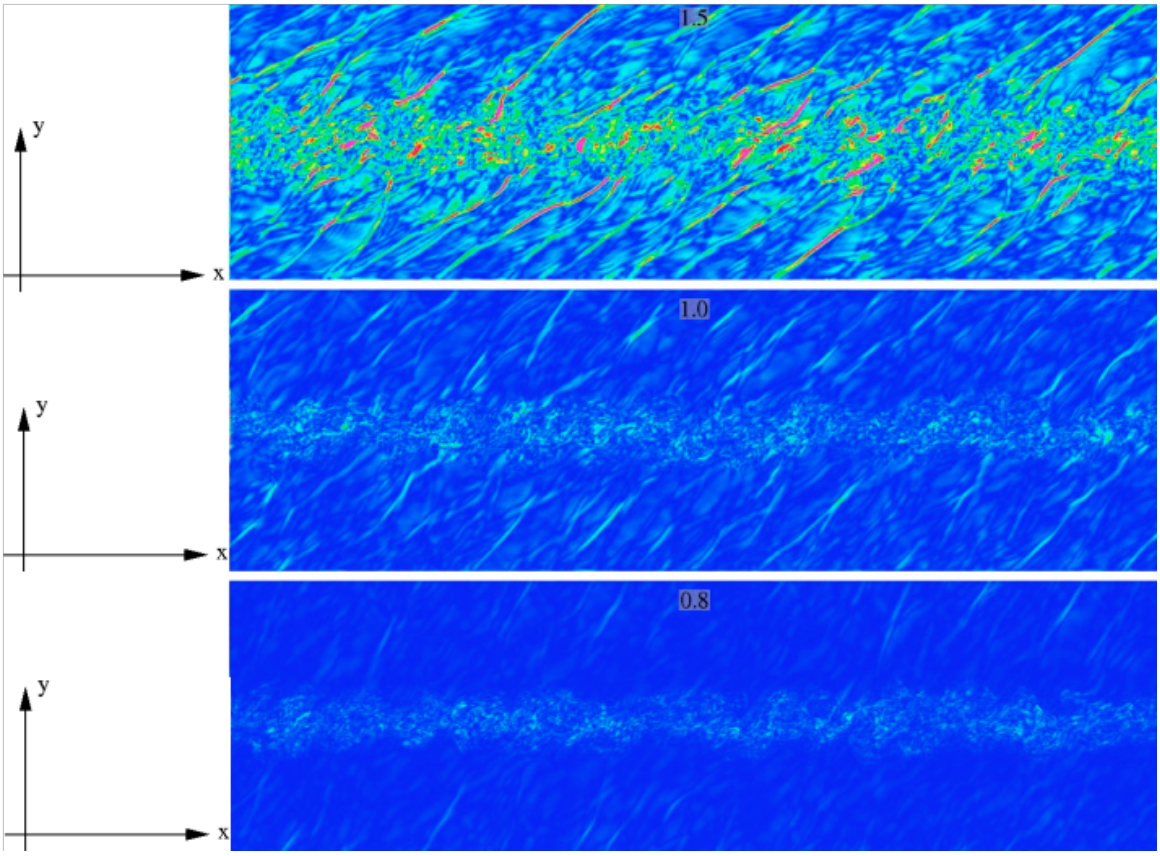

Figure 13: Instantaneous dilatation flow-field at $\tau = 1000$ for three different convective Mach numbers ($M_c = 1.5$, 1.0, and 0.8 from top to bottom). Note that the plot are based on the non-linear dimensionless variable, $\phi = 1 - \tanh\left[\kappa \nabla\cdot \mathbf{u}/(\nabla\cdot \mathbf{u})_{max}\right]$, the parameter $\kappa = 0.5$ governs the amplification of small gradients; a value of κ close to 15 provides good results.

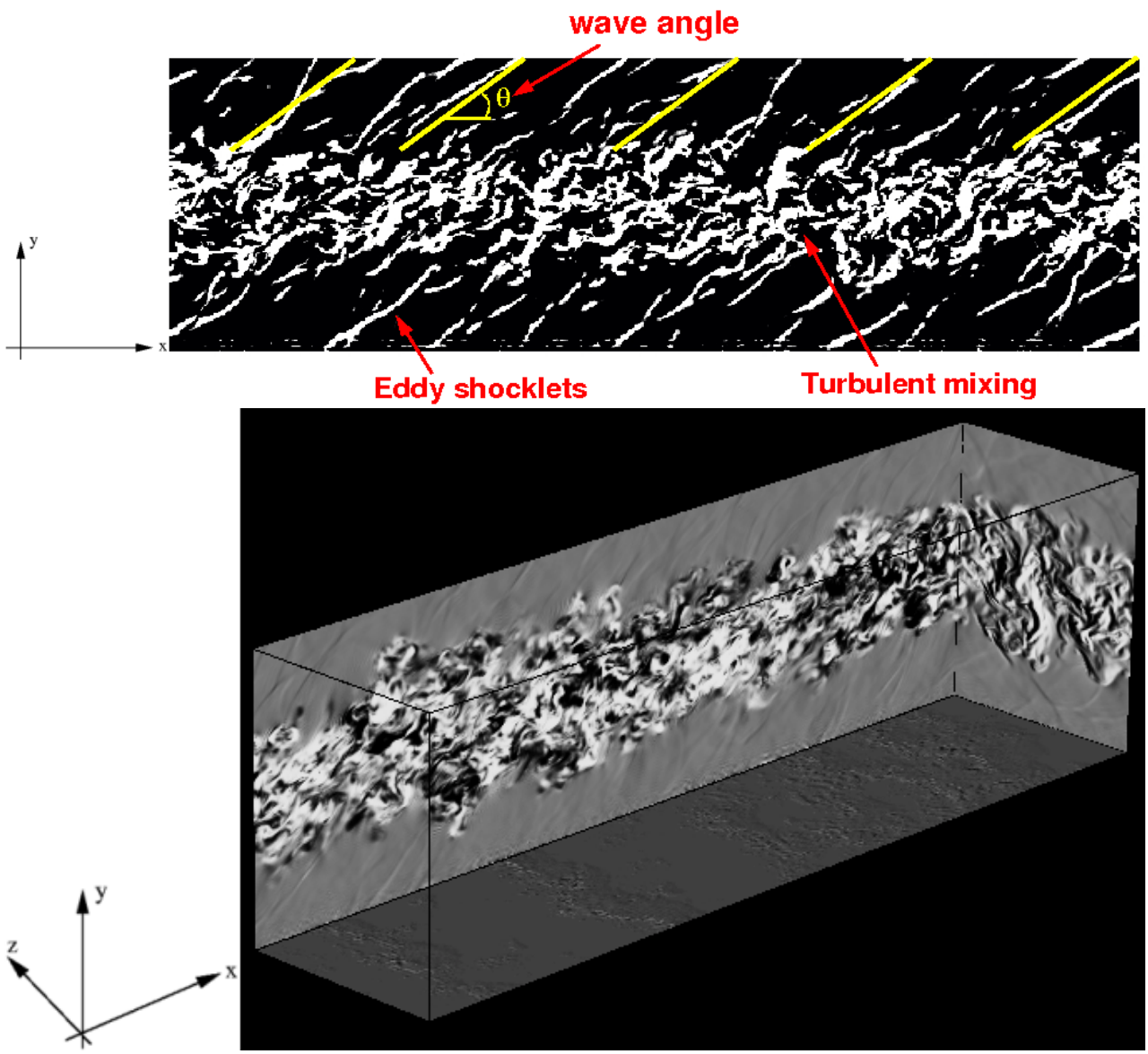

Figure 14: Instantaneous numerical Schlieren pictures at $\tau = 2000$, LES-C5.

6. Acknowledgments

The authors wish to express their gratitude to T. Sandstrom and C. Henze of the Visualization Group, and A. Lazanoff and J. Chang of the Scientific Consultant Group, Code TN, NASA Ames for their help. Special thanks to M. Rogers and A. Wray for their valuable discussion during the course of this research. The support of the DOE/SciDAC SAP grant DE-AI02-06ER25796 is acknowledged. Part of the work by the second author was performed under the NASA Fundamental Aeronautics Hypersonic Program. Work by the third author was performed under the auspices of the U.S. Department of Energy by Lawrence Livermore National Laboratory under Contract DE-AC52-07NA27344.

Appendix A. Subgrid Model

The most widely used and simplest model is Smagorinsky's model [55], which employs an eddy viscosity hypothesis to express the subgrid scale stress as,

$$\tau_{ij} - \frac{1}{3}\tau_{kk}\delta_{ij} = -2\,\mu_t(\widetilde{S}_{ij} - \frac{1}{3}\widetilde{S}_{kk}\delta_{ij})..\tag{19}$$

The eddy viscosity, μ_t, is modeled according to,

$$\mu_t = \overline{\rho}\,C_s\Delta^2|\widetilde{S}|,$$

where C_s is the Smagorinsky constant and $|\widetilde{S}|$ is defined as:

$$|\widetilde{S}| = \left(2\widetilde{S}_{ij}\widetilde{S}_{ij}\right)^{1/2}.$$

The model for the isotropic part of the subgrid scale stress was proposed by Yoshizawa [75] as

$$\tau_{kk} = 2\,C_I\overline{\rho}\,\Delta^2|\widetilde{S}|^2.$$

According to Erlebacher *et al.* [14], τ_{kk} can be neglected in flows where turbulent Mach number, $M_t = \frac{\sqrt{3}\,u_{rms}}{\langle a\rangle}$, is less than 0.4.

The dynamic procedures have been developed to evaluate the parameters used in the subgrid models using the information provided by the resolved scales. The original procedure was developed by Germano *et al.* [19] and later modified by Lilly [31] for incompressible flows. Moin *et al.* [36] generalized the dynamic procedure for compressible flows. The procedure is as follows: The subgrid scale stress for compressible flows which is defined in Eq. 11 can be rewritten as

$$\tau_{ij} = \overline{\rho u_i u_j} - \left(\frac{\overline{\rho u_i}\,\overline{\rho u_i}}{\bar{\rho}}\right).\tag{20}$$

Now the field $\widetilde{u}_i$ is considered as instantaneous field and a test filter with the filter kernel $\widehat{G}(\vec{x}-\vec{y},2\Delta)$ is applied to the LES filtered Navier-Stokes equation to get the resolved turbulent stress,

$$L_{ij} = \left(\widehat{\overline{\rho}\widetilde{u}_i\widetilde{u}_j}\right) - \frac{\widehat{\overline{\rho}\widetilde{u}_i}\,\widehat{\overline{\rho}\widetilde{u}_j}}{\widehat{\overline{\rho}}},\tag{21}$$

where $\widehat{q}$ denotes the test filtered variable q. The subtest stresses are defined by,

$$T_{ij} = \widehat{\overline{\rho} u_i u_j} - \frac{\widehat{\overline{\rho} u_i}\,\widehat{\overline{\rho} u_j}}{\widehat{\overline{\rho}}} \tag{22}$$

From Eqs. 20, 22 and 21, we get the Germano identity,

$$L_{ij} = T_{ij} - \widehat{\tau_{ij}} \tag{23}$$

In the above equation, the two terms on the $r.h.s.$ can be modeled according to Smagorinsky. The term in the $l.h.s.$ can be explicitly calculated by applying the test filter to the simulation results which were obtained using the first filter.

The anisotropic part of the subgrid stress given in Eq. 22 can be modeled according to Smagorinsky as

$$T_{ij} - \frac{1}{3} T_{ll} \delta_{ij} = -2 C_s \widehat{\overline{\rho}} \widehat{\Delta}^2 |\widehat{\widetilde{S}}| \widehat{\widetilde{S}^{\star}_{ij}} \tag{24}$$

with $\widetilde{S}^{\star}_{ij} = \widetilde{S}_{ij} - \frac{1}{3}\widetilde{S}_{ll}\delta_{ij}$. The isotropic part of the subgrid stress given in Eq. 22 can be modeled according to Yoshisawa as

$$T_{ll} = 2 C_I \widehat{\overline{\rho}} \widehat{\Delta}^2 |\widehat{\widetilde{S}}|^2. \tag{25}$$

After applying the test filter to the subgrid stress tensor of $\widetilde{u}_i$ (Eq. 19) and substituting it along with Eq. 24 into Eq. 23, we get,

$$\underbrace{L_{ij} - \frac{1}{3} L_{ll} \delta_{ij}}_{L_{ij}^{Cs}} = C_s \underbrace{\left[-2 \widehat{\overline{\rho}} \widehat{\Delta}^2 |\widehat{\widetilde{S}}| \widehat{\widetilde{S}^{\star}_{ij}} + 2\Delta^2 \left(\left(\widehat{\overline{\rho} |\widetilde{S}| \widetilde{S}_{ij}} \right) - \frac{1}{3} \left(\widehat{\overline{\rho} |\widetilde{S}| \widetilde{S}_{ll}} \right) \delta_{ij} \right) \right]}_{M_{ij}^{Cs}}, \tag{26}$$

$$L_{ll} = C_I \underbrace{\left[2 \widehat{\overline{\rho}} \widehat{\Delta}^2 |\widehat{\widetilde{S}}|^2 - 2\Delta^2 \left(\widehat{\overline{\rho} |\widetilde{S}|^2} \right) \right]}_{M_{ll}^{C_I}}. \tag{27}$$

The above equations can be rewritten in compact form as

$$L_{ij}^{C_s} = C_s M_{ij}^{C_s}, \qquad L_{ll} = C_I M_{ll}^{C_I}. \tag{28}$$

Modifying the original approach by Germano to find C_s and C_I from the above equations, Lilly [31] introduced least square method which gives

$$C_s = \frac{\left\langle L_{ij}^{C_s} M_{ij}^{C_s} \right\rangle_H}{\left\langle M_{ij}^{C_s} M_{ij}^{C_s} \right\rangle_H}, \qquad C_I = \frac{\langle L_{ll} \rangle_H}{\left\langle M_{ll}^{C_I} \right\rangle_H}. \tag{29}$$

In the above equations, as we can see, an averaging is done in the homogenous direction. This is to avoid excessively large local values of C_s and C_I which may destabilize the numerical simulation.

Appendix B. Algorithm for Turbulence Initialization [26]

(a) Choose length scales in each direction $L_x = n_x \Delta x$, $L_y = n_y \Delta y$ and $L_z = n_z \Delta z$

(b) Choose a filter width $N_{f_\alpha} \geq 2n_\alpha$, $\alpha = x, y, z$

(c) Initialize and store random fields $\mathcal{R}_\alpha$ with zero mean and unity variance of dimension $\left[-N_{f_x} : N_{f_x}, -N_{f_y} + 1 : N_{f_y} + N_y, -N_{f_z} + 1 : N_{f_z} + N_z\right]$, where $N_y \times N_z$ are the number of the mesh points in yz plane

(d) Calculate filter coefficients $b(i, j, k)$, where $b_{i,j,k} = b_i \cdot b_j \cdot b_k$,

$$b_k \approx \frac{\tilde{b}_k}{\left(\sum_{j=-Nf}^{Nf} \tilde{b}_j^2\right)^{1/2}} \quad \text{and} \quad \tilde{b}_k = \exp\left(-\frac{\pi k^2}{2n^2}\right)$$

(e) Apply the filter operation for $j = 1, ..., N_y, k = 1, ..., N_z$

$$\mathcal{U}_\alpha(j,k) = \sum_{i'=-N_{fx}}^{N_{fx}} \sum_{j'=-N_{fy}}^{N_{fy}} \sum_{k'=-N_{fz}}^{N_{fz}} b(i',j',k')\, \mathcal{R}_\alpha(i', j+j', k+k')$$

which results in the two-dimensional arrays of spatially correlated data $\mathcal{U}_\alpha$

(f) Perform the following coordinate transformation to get $\mathcal{U'}_\alpha(j,k) = a_{ij}\, \mathcal{U}_\alpha(j,k)$, with prescribed Reynolds stress tensor

$$a_{ij} = \begin{pmatrix} (R_{11})^{1/2} & 0 & 0 \\ R_{21}/a_{11} & (R_{22} - a_{21}^2)^{1/2} & 0 \\ R_{31}/a_{11} & (R_{32} - a_{21}a_{31})/a_{22} & (R_{33} - a_{31}^2 - a_{32}^2)^{1/2} \end{pmatrix}$$

(g) Calculate $u_\alpha(j,k) = \overline{u}_\alpha(j,k) + \mathcal{U'}_\alpha(j,k)$ for first (j,k) plane

(h) Discard the first y, z plane of $\mathcal{R}_\alpha$ and shift the whole data $\mathcal{R}_\alpha(i,j,k) := \mathcal{R}_\alpha(i+1,j,k)$

(i) Generate new random numbers to fill the plane $\mathcal{R}_\alpha(N_{f_x}, j, k)$

(j) Repeat the steps (e) to (i) for each mesh point in the x direction

References

[1] de E. J. Avital, N. D. Sandham and K. H. Luo, *Mach wave radiation by mixing layers. Part I: Analysis of the sound field*, Theor. Comput. Fluid Dyna. **12** (1998) 73.

[2] de E. J. Avital, N. D. Sandham and K. H. Luo, *Mach wave radiation by mixing layers. Part II: Analysis of the sound field*, Theor. Comput. Fluid Dyna. **12** 91 (1998) 91.

[3] M.F. Barone, W.L. Oberkampf and F.G. Blottner, *Validation case study: Prediction of compressible turbulent mixing layer growth rate*, AIAA J., **44** (2006) 1488-1497.

[4] S. Barre, P. Braud, O. Chambres and J.P. Bonnet, *Influence of inlet pressure conditions on supersonic turbulent mixing layers*, Experimental Thermal and Fluid Science, **14** (1997) 68-74.

[5] J. H. Bell and R. D. Mehta, *Development of a two-stream mixing layer from tripped and untripped boundary layers*, *AIAA J.*, **28** (12) (1990) 2034-2042.

[6] A. Bhagatwala and S.K. Lele, *A modied articial viscosity approach for compressible turbulence simulations*, J. Comput. Phys.,

[7] D. W. Bogdanoff, *Compressibility effects in turbulent shear layers*, AIAA J., **21** (1983) 926-927.

[8] O. Chambres, S. Barre, and J.P. Bonnet, *Detailed turbulence characteristics of a highly compressible supersonic turbulent plane mixing layer*. J. Fluid Mech. (1998).

[9] N. Chinzei, G. Masua, T. Komuro, A. Murakami and K. Kudou, *Spreading of two-stream supersonic turbulent mixing layers*, Phys. Fluids **2** (1986) 1345-1347.

[10] J. W. Deardorff, *Three dimensional numerical study of the height and mean structure of a heated planetary boundary layer*, Boundary Layer Meteorol. **7** (1974) 81.

[11] F. Ducros, V. Ferrand, F. Nicoud, C. Weber, D. Darracq, C. Gacherieu, and T. Poinsot, *Large-Eddy Simulation of the Shock/ Turbulence Interaction*, J. Comput. Phys., **152** (1999) 517-549.

[12] F. Ducros, F. Laporte, T. Souleres, V. Guinot, P. Moina and B. Caruelle, *High-order fluxes for conservative skew-symmetric-like schemes in structured meshes: Application to compressible flows*, J. Comput. Phys. **16** (2000) 114139.

[13] G.S. Elliott, M. Samimy, *Compressibility effects in free shear layers*, Phys. Fluids, **2** (1990) 1231-1240.

[14] G. Erlebacher, M. Y. Hussaini, C. G. Speziale and T. A. Zang, *Toward the large eddy simulation of compressible turbulent flows*, J. Fluid Mech., **238** (1992) 155.

[15] M. Farge, G. Pellegrino and K. Schneider *Coherent vortex extraction in 3D turbulent flows using orthogonal wavelets*, Phys. Rev. Lett., **5** (2001) 45011-45014.

[16] H. Foysi and S. Sarkar, *The compressible mixing layer: an LES study*, Theor. Comp. Fluid Dyn., DOI: 10.1007/s00162-009-0176-8 (2010).

[17] J. B. Freund, S. K. Lele and P. Moin, *Compressibility effects in a turbulent annular mixing layer. Part 1. Turbulence and growth rate*, J. Fluid Mech. 421 (2000) 229-267.

[18] B. Galperin and S. A. Orszag, *Large eddy simulation of complex engineering and geophysical flows*, Cambridge University Press, (1993).

[19] M. Germano, U. Piomelli, P. Moin, and W. H. Cabot, *A dynamic subgrid-scale eddy viscosity model*, Phys. Fluids **A 3** (1991) 1760.

[20] M.R. Gruber, N.L. Messersmith and J.C. Dutton, *Three dimensional velocity field in a compressible mixing layer*, AIAA Journal, **31** (1993) 2061-2067.

[21] A. Hadjadj and A. Kudryavtsev, *Computation and flow visualization in high speed aerodynamics*, *J. Turbul.* , **6** (2005) 33-81.

[22] A. Hadjadj and S. Dubos, *Large eddy simulation of supersonic boundary layer at M=2.4*, Proceeding of the IUTAM Symposium on Unsteady Separated Flows and their Control, M. Braza and K. Hourigan (Ed.) Springer, e-ISBN 978-1-4020-9898-7 (2009).

[23] A.H. Honein and P. Moin *Higher entropy conservation and numerical stability of compressible turbulence simulations*, J. Comput. Phys., **201** (2004) 531-545.

[24] G.-S. Jiang and C.-W. Shu, *Efficient implementation of weighted ENO schemes*, J. Comput. Phys., **126** (1996) 202-228.

[25] E. Johnsen, J. Larson, A. V. Bhagatwala, W. H. Cabot, P. Moin, B. J. Olson, P. S. Rawat, S. K. Shankar, B. Sjögreen, H. C. Yee, X. Zhong and S. K. Lele, *Assessment of high-resolution methods for numerical simulations of compressible turbulence with shock waves*, J. Comput. Phys. **229** (2010), 1213-1237.

[26] M . Klein, A. Sadiki, and J. Janicka, *A digital filter based generation of inflow data for spatially developing direct numerical or large eddy simulation*, J. Comp. Phys., **186** (2003) 652-665.

[27] D. Kotov, H.C. Yee, B. Sjögreen, W. Wang and C.W. Shu, *Performance of Four High Oder Shock-Capturing Schemes for Stiff Source Terms with Discontinuities: Preliminary Results*, CTR Annual Technical Brief, Stanford University, October, 2011.

[28] W. L. Oberkampf and M.F. Barone, *Measures of agreement between computation and experiment: Validation metrics*, J. Comp. Phys., **217** (2006) 5-36.

[29] M. Lesieur and O. Metais, *New trends in large-eddy simulations of turbulence*, Ann. Rev. Fluid Mech. **28** (1996) 45-82.

[30] X.-S Li and C.-W. Gu, *An All-speed Roe-type scheme and its ssymptotic analysis of low Mach number behaviour,* J. Comput. Phys., **227** (2008) 5144-5159.

[31] D. K. Lilly, *A proposed modification of the Germano subgrid-scale closure method*, Phys. Fluid **4** (1992) 633.

[32] S.-C. Lo, G.A. Blaisdell and A.S. Lyrintzis *High-order shock capturing schemes for turbulence calculations*, Int. J. Numer. Meth. Fluids **62** (2010) 473-498.

[33] I. Mahle, J. Sesterhenn and R. Friedrich, *Turbulent mixing in temporal compressible shear layers involving detailed diffusion processes*, *J.Turb.*, **8** (2007) 1-2.

[34] C. Meneveau and J. Katz, *Scale-invariance and turbulence models for large-eddy simulation*, Ann. Rev. Fluid Mech. **32** (2000) 1-32.

[35] S. B. Pope, *Turbulent flows*, Cambridge University Press, Cambridge, (2000).

[36] P. Moin, K. Squires, W. Cabot and S. Lee, *A dynamic subgird scale model for compressible turbulence and scalar transport*, Phys. fluids **3** (1991) 2746.

[37] P. L. O'Neill, D. Nicolaides, D. Honnery and J. Soria, *Autocorrelation functions and the determination of integral length with reference to experimental and numerical data*, Proc. of the 15th Australasian Fluid Mech. Conf. The Univ. of Sydney, Australia, 13-17 Dec. (2004).

[38] P. Olsson and J. Oliger, *Energy and maximum norm estimates for nonlinear conservation laws*, RIACS Technical Report 94.01 (1994).

[39] C. Pantano and S. Sarkar, *A study of compressible effects in the high-speed turbulent shear layer using direct simulation*, J. Fluid Mech., **451** (2002) 329-371.

[40] D. Papamoschou and A. Roshko, *The compressible turbulent shear layer: An experimental study*, J. Fluid Mech., **197**, (1988) 453-477.

[41] D. Papamoschou, *Model for entropy production and pressure variation in confined turbulent mixing layer*, *AIAA J.*, **31** (1993) 1643-1650.

[42] S. B. Pope, *Ten questions concerning the large eddy simulation of turbulent flows*, New Journal of Physics **6** (2004) 35.

[43] P.L. Roe, *Approximate Riemann solvers, parameter vectors, and difference schemes*, J. Comput. Phys., **43** (1981) 357-372.

[44] R. S. Rogallo, P. Moin, Numerical Simulation of Turbulent Flows, Ann. Rev. Fluid Mech. **18**, 99-137 (1984).

[45] M. M. Rogers and R. D. Moser, *Direct simulation of a self-similar turbulent mixing layer*, Phys. Fluids, **6** (1994) 903-923.

[46] P. Sagaut, *Large eddy simulation of turbulent flows*, Springer, Berlin, (2001).

[47] P. Sagaut and M. Germano, *On the Filtering Paradigm for LES of Flows with Discontinuities*, J. Turbulence, **6** (2005), 1-9.

[48] M. Samimy and G.S. Elliot, *Effect of compressibility on the characteristics of free shear layer*, AIAA J., **28** (1990) 439-445.

[49] M. Samimy, M.F. Reeder and G.S. Elliott, *Compressibility effects on large structures in free shear flows*, Phys. Fluids, **4** (1992) 1251-1258.

[50] N. D. Sandham and W. C. Reynolds, *A numerical investigation of the compressible mixing layer*, Stanford Rep. TF-45 (1989).

[51] B. Sjögreen and H. C. Yee, *Multiresolution Wavelet Based Adaptive Numerical Dissipation Control for Shock-Turbulence Computation*, J. Scient. Computing, **20** (2004), 211–255.

[52] B. Sjögreen, H.C.Yee, M.J.Djomehri, A.Lazanoff, and W.D.Henshaw, *Parallel Performance of ADPDIS3D - A High Order Multiblock Overlapping Grid Solver for Hypersonic Turbulence*, Proceedings of the 21st International Conference on Parallel CFD, Moffett Field, CA, May 18-22, 2009.

[53] B.Sjögreen and H.C.Yee, *Variable High Order Multiblock Overlapping Grid Methods for Mixed Steady and Unsteady Multiscale Viscous Flows*, Commun. Comput. Phys., **5** (2009), pp. 730–744.

[54] B. Sjögreen and H. C. Yee, *On skew-symmetric splitting of the Euler equations*, Proceedings of the EUNUMATH-09 Conference, June 29 - July 2, 2009, to appear.

[55] J. Smagorinsky, *General circulation experiments with the primitive equations. I. the basic experiment*, Mon. Weather Rev **91** (1963) 99.

[56] B. W. Spencer and B. Jones, *Statistical investigation of pressure and velocity fields in the turbulent two-stream mixing layer*, AIAA Paper 71-613 (1971).

[57] A. Stuart and A.R. Humphries (*Dynamical systems and numerical analysis*, Cambridge Monographs on Applied and Computational Mathematics, 1998.

[58] B. Vreman, N. Sandham and K.H. Luo, *Compressible mixing layer growth rate and turbulence characteristics*, J. Fluid Mech. **320** (1996 235-258.

[59] W. Wang, H.C. Yee, B. Sjögreen, T. Magin and C.W. Shu, *Construction of low dissipative high-order well-balanced lter schemes for nonequilibrium ows*, J. Comput. Phys., to appear 2010 (doi:10.1016/j.jcp.2010.04.033, 2010).

[60] W. Wang, C.W. Shu, H.C. Yee and B. Sjögreen, *High Order Finite Difference Methods with Subcell Resolution for Advection Equations with Stiff Source Terms*, J. Comput. Physics, **231** (2012) 190214.

[61] H.C. Yee, J.R. Torczynski, S.A. Morton, M.R. Visbal, and P.K. Sweby, *On Spurious Behavior of CFD Simulations*, AIAA 97-1869, Proceedings of the 13th AIAA Computational Fluid Dynamics Conference, June 29 - July 2, 1997, Snowmass, CO.; also Int. J. Num. Meth. Fluids, **30** (1999) 675-711.

[62] H.C. Yee and P.K. Sweby, *Dynamics of Numerics & Spurious Behaviors in CFD Computations*, Keynote paper, 7th ISCFD Conference, Sept. 15-19, 1997, Beijing, China, RIACS Technical Report 97.06, June 1997.

[63] H.C. Yee, N.D. Sandham, N.D., and M.J. Djomehri, *Low dissipative high order shock-capturing methods using characteristic-based filters*, J. Comput. Phys., **150** (1999) 199-238.

[64] H.C. Yee, M. Vinokur, M., and M.J. Djomehri, *Entropy splitting and numerical dissipation*, J. Comput. Phys., **162** (2000) 33-81.

[65] H.C. Yee and B. Sjögreen, *Designing Adaptive Low Dissipative High Order Schemes for Long-Time Integrations*, In Turbulent Flow Computation, (Eds. D. Drikakis & B. Geurts), Kluwer Academic Publisher (2002); also RIACS Technical Report TR01-28, Dec. 2001.

[66] H.C. Yee, *Building Blocks for Reliable Complex Nonlinear Numerical Simulations*, In Turbulent Flow Computation, (Eds. D. Drikakis & B. Geurts), Kluwer Academic Publisher (2002); also RIACS Technical Report TR01-28, Dec. 2001.

[67] H.C. Yee and B. Sjögreen, *Efficient low dissipative high order scheme for multiscale MHD flows, II: Minimization of div(B) numerical error*, RIACS Technical Report TR03.10, July, 2003, NASA Ames Research Center; also, J. Scient. Computing, **29** (2006) 115-164.

[68] H.C. Yee and B. Sjögreen, *Development of low dissipative high order filter schemes for multiscale Navier-Stokes/MHD systems*, J. Comput. Phys., **225** (2007) 910-934.

[69] H. C. Yee, B. Sjögreen, and M. Barone, *High order numerical schemes for hypersonic flow simulations*, VKI Lecture Series. Course on Hypersonic Entry and Cruise Vehicles, 30 June - 3 July 2008.

[70] H.C. Yee and B. Sjögreen, *High order filter methods for wide range of compressible flow speeds*, Proceedings of ICOSAHOM 09 (International Conference on Spectral and High Order Methods). June 22-26, 2009, Trondheim, Norway.

[71] H.C. Yee, B. Sjögreen and A. Hadjadj, *Comparative Study of High Order Schemes for LES of Temporal-Evolving Mixing Layers*, Proceedings of ASTRONUM-2010, June 13-18, 2010, San Diego, Calif.

[72] H.C. Yee and B. Sjögreen, *Local Flow Sensors in Controlling Numerical Dissipations for a Wide Spectrum of Flow Speed and Shock Strength*, in preparation.

[73] H.C. Yee, B. Sjögreen, C.W. Shu, W. Wang, T. Magin and A. Hadjadj, *On Numerical Methods for Hypersonic Turbulent Flows*, Proceedings of ESA 7th Aerothermodynamics Symposium, 9 - 12 May 2011 Site Oud Sint-Jan, Brugge, Belgium.

[74] H.C. Yee, D. Kotov, B. Sjögreen, W. Wang and C.W. Shu, *Numerical Dissipation and Wrong Propagation Speed of Discontinuities For Stiff Source Terms*, Proceedings of the ASTRONUM-2011, Valencia, Spain, June 13-17, 2011.

[75] A. Yoshizawa, *Statistical theory for compressible turbulent shear flows, with the application to subgrid modeling*, Phys. Fluids, **29** (1986) 2152.